M. Tugnoli, D. Montagnani, M. Syal, G. Droandi, A. Zanotti
Mid-Fidelity Approach to Aerodynamic Simulations of Unconventional VTOL Aircraft Configurations
Aerospace Science and Technology, Vol. 115, 2021, 106804 (17 pages)
doi:10.1016/j.ast.2021.106804

Mid-Fidelity Approach to Aerodynamic Simulations of Unconventional VTOL Aircraft Configurations

Matteo Tugnoli[a,1], Davide Montagnani[a,1], Monica Syal[b,3], Giovanni Droandi[b,1], Alex Zanotti[a,4,*]

[a]*Politecnico di Milano, Department of Aerospace Science and Technology, Milan, Italy*
[b]*A^3 by Airbus LLC, Sunnyvale, California, U.S.A.*

Abstract

A new flexible medium-fidelity open source computational tool was developed with the purpose of obtaining fast and reliable aerodynamic simulations of unconventional Vertical Take-Off and Landing (VTOL) aircraft configurations, such as the emerging category of eVTOLs. This tool, called `DUST`, ensures quick simulations and provides reasonably accurate results when the need for numerous evaluations rules out an extensive use of CFD due to its high computational cost, while maintaining robustness in the complex interactional aerodynamic phenomena typical of the novel eVTOL configurations. The paper first presents the analytical formulation of the tool, based on different potential boundary elements and a vortex particles wake integrated in a common formulation. Then, the results obtained with the novel code are compared with experimental data and CFD results of a half-span tiltwing tiltrotor model and an eVTOL multi-rotor tiltwing aircraft, both in hover and forward flight mode. The comparisons show that DUST produces

*Corresponding author
Email address: `Alex.Zanotti@polimi.it` (Alex Zanotti)
[1]Post-Doctoral Research Fellow
[2]Senior Aerodynamics Engineer
[3]Flight Physics and Pre-Design Lead
[4]Assistant Professor

results that are as accurate as the results obtained with CFD, except for massively separated conditions, at a computational cost orders of magnitude lower. The results highlight the effectiveness of this approach for the preliminary design of a vehicle and for the preliminary study of the flow physics related to the aerodynamic interactions between rotor wakes and solid bodies as wings.
Keywords: Mid-fidelity aerodynamics, Vortex particle method, eVTOL, Tiltrotor

Notation

c	chord
C_P	power coefficient $C_P = Q/(\rho\Omega^2 R^5\pi)$
C_T	thrust coefficient $C_T = T/(\rho\Omega^2 R^4\pi)$
FM	figure of merit $FM = C_T^{3/2}/(C_P\sqrt{2})$
L	aircraft lift
LL	lifting line
M	Mach number
P_a	available power
P_s	shaft power
Q	rotor torque
Re	Reynolds number
SP	surface panel
t	time
T	rotor thrust
$\boldsymbol{U}_\infty$	free stream velocity
$\boldsymbol{u}_\phi$	potential velocity
$\boldsymbol{u}_\varphi$	potential perturbation velocity
$\boldsymbol{u}_\psi$	rotational perturbation velocity
VL	vortex lattice
V_z	vertical flight velocity
V_∞	free stream flight velocity
W	aircraft weight
α	angle of attack
$\vec{\alpha}$	vortex particle intensity
μ	surface doublet intensity
σ	surface source intensity

ϕ	velocity potential
φ	perturbation velocity potential
Γ	circulation of lifting line
$\boldsymbol{\psi}$	vector potential
ρ	density
σ	rotor solidity
τ_S	rotor shaft angle
τ_W	outboard wing tilting angle
θ	collective pitch angle
θ_{1C}	lateral cyclic pitch angle
θ_{1S}	longitudinal cyclic pitch angle
Ω	rotor speed
$\boldsymbol{\omega}$	vorticity
Ω_f	fluid domain
Ω_φ	fluid domain for the potential velocity

Indices

$()_b$	body variables
$()_s$	contributions from body surface panels
$()_v$	contributions from body vortex lattice elements
$()_l$	contributions from body lifting lines
$()_w$	contributions from wake panels
$()_{\tilde{w}}$	contributions from explicit wake panels

1. Introduction

Recent advances in the field of high performance computing favoured the use of high fidelity Computational Fluid Dynamics (CFD) simulations to obtain both an accurate evaluation of the aerodynamic performance of VTOL aircraft and a deep insight into the complex interactional aerodynamic phenomena typical of these vehicles. Several CFD codes as elsA [1] by ONERA, FLOWer [2] by DLR and Airbus Helicopters Deutschland, HBM3 by University of Glasgow [3] and ROSITA [4] by Politecnico di Milano were developed in Europe with this aim. These codes, based on a finite volume implementation of the Reynolds Averaged Navier-Stokes (RANS) equations, block-structured grids, and Chimera technique were widely used to perform aerodynamic simulations of both helicopters [5] and tiltrotors [6, 7] showing good agreement with wind tunnel measurements. Nevertheless, time-accurate RANS simulations of a VTOL aircraft are still incredibly time consuming and require a huge amount of computational resources. Thus, high-fidelity CFD tools are usually devoted to a limited number of detailed analyses but they are still not suitable to be used in the design process of a new VTOL aircraft due to the large number of aerodynamic simulations required for this task. Consequently, a mid-fidelity numerical approach combining different models represents the best option for the designers of novel VTOL aircraft.

Several mid-fidelity aerodynamic codes were developed in recent years to support the design process of rotary wing aircraft. Just to cite an example, DLR developed UPM [8] an unsteady panel and free-wake code originally intended for aeroacoustic simulations of helicopters but recently applied on arbitrary complex configurations as compound rotorcraft [9].

To achieve a better representation of the aerodynamic characteristics of

a rotor and to better capture rotor-airframe aerodynamic interactions, the vortex particle method (VPM) [10, 11] has been widely used in recent years. Recent literature shows several works employing the VPM for the simulations of rotorcraft applications. For example, Su et al. [12] investigated the aerodynamic characteristics of an electrically controlled rotor using an analysis model based on the viscous VPM.

Lu et al. [13] developed a method for the optimization of the layout of a helicopter using an aerodynamic model based on viscous VPM combined with an unsteady panel hybrid method capable of simulating the interactions between the various components of the helicopter.

The GENeral Unsteady Vortex Particle (GENUVP), a software based on a panel method coupled with a VPM solver, was developed at the National Technical University of Athens (NTUA) for both aerodynamic and aeroacoustic simulations of rotorcraft [14].

An unsteady aerodynamic analysis method based on VPM was recently developed for the investigation of the complex wake of coaxial rotors in the work by Tan et al. [15]. A vortex-based approach coupled with a viscous boundary model was used by the same authors to investigate complex rotorcraft-to-rotorcraft interference problems that occur during shipboard operations, i.e. the flow field and unsteady airloads of a tiltrotor affected by the wake of an upwind tandem rotor [16].

In recent years a growing interest in creating a novel short-range personal concept of aviation as an effective alternative to ground transportation in overcrowded metropolitan areas led to a significant increase in development efforts around the design of new VTOL aircraft. While the development of such new vehicles based on electric distributed propulsion (commonly referred as electric Vertical Take-Off and Landing vehicles or eVTOL) was driven by

the mature state of different technological areas such as electric motors and batteries [17], these new aircraft architectures pose unprecedented challenges to engineers in several different areas.

Mission and safety requirements of such eVTOLs drive the vehicle design towards multi-rotor and multi-wing architectures. The aerodynamics of these new concepts is generally dominated by complicated rotors-wing-airframe interactions that are difficult to simulate and predict. Mid-fidelity tools offer an optimal trade-off between computational cost and desired accuracy, particularly in the preliminary stages of the design, as they allow the engineers to investigate the behaviour of the vehicles by taking into consideration complex aerodynamic interactions otherwise impossible to account for. Alvarez and Ning [18] recently investigated the accuracy of the viscous VPM in modelling rotor-on-rotor aerodynamic interactions in a side-by-side rotor configuration typical of eVTOLs architectures.

The present paper describes the result of a collaboration between Politecnico di Milano and A^3 by Airbus LLC aimed at the development of a new flexible mid-fidelity computational tool called `DUST` [19, 20]. `DUST` provides several models for both aircraft components and wake evolution to obtain fast and reliable aerodynamic simulations of VTOL aircraft of arbitrary configurations. `DUST` is an open source code developed under MIT license. The code exploits the Object Oriented paradigms of the latest Fortran standards to obtain a coherent formulation of the aerodynamic problem, simultaneously involving different modelling techniques. The mathematical formulation of the problem, which is described in details in this paper, relies on the Helmholtz's decomposition of the velocity field to recast the aerodynamic problem as a combination of a boundary value problem for the potential part of the velocity and a mixed panels-vortex particles model of the free

vorticity in the flow. The mixed panel wake-vortex particle model provides a stable Lagrangian description of the free vorticity field in the flow, suitable for numerical simulations with strong aerodynamic interactions.

The assessment of different levels of modelling fidelity for test cases characterised by interactional aerodynamics has become a widely investigated topic in the recent literature. For instance, Mishra et al. [21] compared RANS and VPM modelling against experiments for the study of the interaction of trailing vortices provided by a wing or a propeller with lifting surfaces. A preliminary assessment of `DUST` code capabilities for the simulation of conventional aerodynamic configurations, like airliner models or rotors was provided in a previous work [22] by means of comparison against data available in the literature. The main goal of the present work is to assess accuracy and limitations of `DUST` when used to simulate complex VTOL vehicles as tiltrotors and eVTOLs. In the present paper the `DUST` results are compared with both experimental measurements and high-fidelity numerical simulations over two VTOL aircraft test cases of increasing complexity, i.e. a half-span tiltwing tiltrotor model investigated at Politecnico di Milano in the past years [23] and the Vahana eVTOL multi-rotor tiltwing technology demonstrator built by A^3 by Airbus LLC [24]. Both hover and forward flight conditions are considered.

This paper is organized as follows. The general architecture of the code, the mathematical formulation of the aerodynamic problem and the numerical approach implemented in `DUST` for the description of the flow field and the computation of loads on solid bodies are described in Sec. §2. The results obtained with `DUST` on the selected test cases are presented and compared with CFD simulations and experimental measurements in Sec. §3. Accuracy and limits of validity of aerodynamic analyses performed with `DUST` on com-

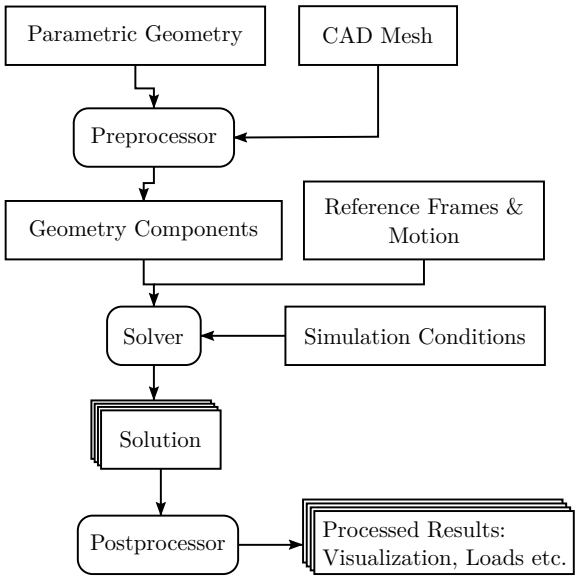

Figure 1: Workflow of DUST

plex VTOL aircraft configurations are discussed in Sec. §4 where conclusions are also drawn.

2. Structure and formulation of the DUST code

The code is divided in a pre-processor, a solver and a post-processor. The typical workflow is depicted in Fig. 1.

The pre-processor allows to import components from pre-existing mesh files. Alternatively, the user can generate components parametrically by specifying the geometry in the input files. The mathematical formulation of the solver is limited to rigid bodies and doesn't allow to simulate flexible components. No volume grid is required, since solid bodies are modelled as a surface distribution of singularities. Different aerodynamic models ranging from the one-dimensional lifting lines and actuator disks, to zero-thickness lifting surfaces and three-dimensional surface panels, are implemented and available in DUST. The intensity of the singularities is determined as the so-

lution of the boundary value problem for the potential part of the velocity vector, supplied with the non-penetration boundary condition. The components are positioned in space and set in motion by defining a hierarchy of reference frames.

The inputs to the solver are: (1) the geometry and the mesh of each components, (2) the reference frames and (3) the simulation conditions and the solver parameters. The solver evolves the simulation in time for the prescribed amount of steps and writes the solution to screen or files as specified by the user. The Kutta condition is enforced by shedding wake from the trailing edges of the lifting bodies, which are automatically detected by the solver using the geometry. The user can choose between a structured vortex lattice wake, a vortex particles wake or a mixed one, which in all cases can evolve in a rigid way with the free stream or be free to evolve with the local flow.

The code is based on the hypothesis of incompressible potential flow. However, compressibility effects can be taken into account for steady aerodynamic loads on surfaces by applying a Prandtl-Glauert correction for surface panels and vortex lattice elements, while using Mach-depending tabulated data for lifting lines elements. `DUST` also provides a flexible postprocessor to produce a vast series of insights on the solution as well as routines for data visualization. The code is written by using the latest standards of Fortran, exploiting object-oriented capabilities to obtain flexibility yet maintaining high computational performance, aided by an extensive OpenMP parallelization.

The mathematical formulation of the aerodynamic solver relies on a vorticity-velocity formulation of the aerodynamic problem, founded on the Helmholtz's decomposition of the velocity field and a Lagrangian description of the vorticity field (see e.g. [25]). The Helmholtz's decomposition of the velocity

field states that the velocity field $\boldsymbol{u}(\boldsymbol{r},t)$ can be written as the sum of an irrotational field, the potential velocity which will be bound to the potential based elements, $\boldsymbol{u}_\phi = \boldsymbol{\nabla}\phi$, and a soleinoidal field, the rotational velocity which will be bound to the particles wake, $\boldsymbol{u}_\psi = \boldsymbol{\nabla} \times \boldsymbol{\psi}$,

$$\boldsymbol{u}(\boldsymbol{r},t) = \boldsymbol{u}_\phi(\boldsymbol{r},t) + \boldsymbol{u}_\psi(\boldsymbol{r},t) \ . \tag{1}$$

The potential velocity is bound to the classical potential-based elements, while the rotational velocity is bound to the vortex particles, which thanks to (1) can be included in a single formulation. The incompressibility condition and the Helmoltz decomposition lead to two problems for the potential velocity ϕ and the vector potential $\boldsymbol{\psi}$,

$$\nabla^2\phi = 0, \tag{2}$$

$$-\nabla^2\boldsymbol{\psi} = \boldsymbol{\omega}, \tag{3}$$

while the Lagrangian description of the dynamical equation governing the vorticity field $\boldsymbol{\omega}(\boldsymbol{r},t)$ of a incompressible flow can be written as

$$\frac{D\boldsymbol{\omega}}{Dt} = (\boldsymbol{\omega}\cdot\boldsymbol{\nabla})\boldsymbol{u} + \nu\nabla^2\boldsymbol{\omega} \ , \tag{4}$$

where ν is the kinematic viscosity of the flow and the material derivative of the vorticity field $D\boldsymbol{\omega}/Dt$ represents the time derivative of the vorticity associated with a material particle. The equations are written in a reference frame moving with a uniform velocity $\boldsymbol{U}_\infty$ with respect to still air, i.e. a uniform free stream velocity with respect to the reference frame is considered. The free stream velocity can also be set to zero to simulate cases without free stream flow conditions.

The differential problems defined in the fluid domain Ω_f are manipulated using Green's function method, in order to obtain a volume-grid free formulation of the aerodynamic problem.

While the rotational velocity is generated by the wake vortex particles which will be described in section 2.5, the potential velocity field is generated by a set of different classical singular surface elements.

The solution of Eq. (2) for the velocity potential relies on the superposition principle of surface elementary singularities, associated with the aerodynamic element types: surface panels, vortex rings and lifting lines, and the part of the wake which is modelled by panels. The fluid domain Ω_φ is delimited by the aerodynamic elements and wake $\partial\Omega_\varphi = S_b \cup S_w = S_s \cup S_v \cup S_l \cup S_w$. Each element type is defined by its singularity distribution, its boundary condition and load computation. Vortex ring elements also provide the model for the surface S_w of the potential part of the wake, i.e. the part modelled by panels. Note that vortex rings and uniform doublet panels are equivalent, as indicated in Secs. 2.3 and 2.5. Surface panels provide the aerodynamic elements for modelling the surface S_s of solid thick bodies. Vortex lattice elements provide a zero-thickness model for the surface S_v of thin lifting bodies with a distribution of vortex rings. Lifting line elements provide a 1-D line vortex model for thin lifting bodies (see 2.4), with tabulated sectional aerodynamic coefficients naturally including the viscous effects. In particular, S_l is the surface of the thin lifting bodies represented aerodynamically by a lifting line model and constitutes its first panel wake portion. The problem is reformulated using the perturbation velocity potential $\varphi := \phi - \phi_\infty$ and the perturbation potential velocity $\boldsymbol{u}_\varphi = \boldsymbol{\nabla}\varphi = \boldsymbol{u}_\phi - \boldsymbol{U}_\infty$, leading to the Laplace equation for the perturbation velocity potential

$$\nabla^2\varphi = 0 \qquad \text{in } \Omega_\varphi \ , \tag{5}$$

supplemented with the far-field boundary condition,

$$\varphi \to 0 \qquad |\boldsymbol{r}| \to \infty \ , \tag{6}$$

where $\boldsymbol{U}_\infty$ and ϕ_∞ are the free stream velocity and its potential.

2.1. Boundary Integral Equation

Loosely following the classical Morino formulation (see e.g [26]), Eq. (5) is recast as a boundary element problem using Green's function method,

$$\begin{aligned} E(\boldsymbol{r})\varphi(\boldsymbol{r},t) = &+ \oint_{S_s} \hat{\boldsymbol{n}}(\boldsymbol{r_0},t)\cdot\boldsymbol{\nabla_0} G(\boldsymbol{r_0},\boldsymbol{r})\,\varphi(\boldsymbol{r_0},t)\;dS(\boldsymbol{r_0}) \\ &+ \int_{\partial\Omega_\varphi\backslash S_s} \hat{\boldsymbol{n}}(\boldsymbol{r_0},t)\cdot\boldsymbol{\nabla_0} G(\boldsymbol{r_0},\boldsymbol{r})\,\Delta\varphi(\boldsymbol{r_0},t)\;dS(\boldsymbol{r_0}) \\ &- \oint_{S_s} G(\boldsymbol{r_0},\boldsymbol{r})\,\hat{\boldsymbol{n}}(\boldsymbol{r_0},t)\cdot\boldsymbol{\nabla_0}\varphi(\boldsymbol{r_0},t)\;dS(\boldsymbol{r_0})\;. \end{aligned} \tag{7}$$

$\hat{\boldsymbol{n}}(\boldsymbol{r_0},t)$ is the unit normal vector on the surfaces $\partial\Omega_\varphi$, pointing outward the solid bodies on S_s, and $\partial\Omega_\varphi\backslash S_s$ is the whole boundary domain excluding the solid bodies surfaces. $G(\boldsymbol{r_0},\boldsymbol{r}) = 1\,/\,(4\pi|\boldsymbol{r}-\boldsymbol{r_0}|)$ is the Green's function of the Laplace problem in the three-dimensional space, and $E(\boldsymbol{r})$ is the indicator function of the fluid domain Ω_φ

$$E(\boldsymbol{r}) = \begin{cases} 1\;, & \boldsymbol{r}\in\Omega_\varphi \\ \dfrac{1}{2}\;, & \boldsymbol{r}\in\partial\Omega_\varphi \\ 0\;, & \boldsymbol{r}\notin\Omega_\varphi \quad . \end{cases} \tag{8}$$

The surface integral in Eq. (7) has been split into the contribution of thick bodies and of the rest of the thin surfaces, where only the jump of the potential $\Delta\varphi$ is defined.

The formulation in Eq.(7) can be interpreted as the superposition principle for the perturbation velocity potential, identifying in the Green's function $G(\boldsymbol{r_0},\boldsymbol{r})$ and the term $\hat{\boldsymbol{n}}(\boldsymbol{r_0},t)\cdot\boldsymbol{\nabla_0}G(\boldsymbol{r_0},\boldsymbol{r})$ the opposite of the velocity potential induced in $\boldsymbol{r}$ by a unitary source and a unitary doublet singularity located in $\boldsymbol{r_0}$, respectively. Note that the gradient $\boldsymbol{\nabla_0} = \partial/\partial r_{0,i}$ differently

from $\boldsymbol{\nabla} = \partial/\partial r_i$ is performed with respect to the integration variable $\boldsymbol{r_0}$ ($\partial/\partial r_i = -\partial/\partial r_{0,i}$). The problem in Eq. (7) is complemented by the Neumann's non-penetration boundary condition on the surface S_s, $\hat{\boldsymbol{n}} \cdot \boldsymbol{u} = \hat{\boldsymbol{n}} \cdot \boldsymbol{u}_b$, which can be written as

$$\hat{\boldsymbol{n}} \cdot \boldsymbol{u}_\varphi = \hat{\boldsymbol{n}} \cdot \boldsymbol{\nabla}\varphi = \hat{\boldsymbol{n}} \cdot (\boldsymbol{u}_b - \boldsymbol{U}_\infty - \boldsymbol{u}_\psi) =: \sigma(\boldsymbol{u}_\psi; \boldsymbol{U}_\infty, \boldsymbol{u}_b) \ , \qquad \text{on } S_s \quad (9)$$

where $\boldsymbol{u}_b$ represents the motion of the surface S_s, which, as the rest of the formulation, is relative to a reference frame subject to a free stream velocity $\boldsymbol{U}_\infty$. A doublet distribution is associated with the whole boundary $\partial\Omega_\varphi$ of the fluid domain for the potential velocity, while S_v, S_l and S_w have no source contribution because of the continuity of normal velocity boundary conditions on both sides of zero-thickness surfaces.

2.2. Surface panels (SP)

The surface panels are used to model solid bodies with thickness, and their formulation follows [26]. Boundary integral Eq. 7 is solved by the collocation method. The surfaces of solid bodies S_b, the thin surfaces with no thickness and the potential part of the wake S_w (i.e., that is surface based and not the particles wake) are subdivided into panels. Using a uniform-intensity panel discretisation and defining the intensity of the doublets, $\mu_{i_s} = -\varphi_{i_s}$, and the sources, $\sigma_{i_s} = \hat{\boldsymbol{n}}_{i_s} \cdot (\boldsymbol{u}_b - \boldsymbol{U}_\infty - \boldsymbol{u}_\psi)_{i_s}$ on the surface panels and again the doublets intensity on the thin surfaces $\mu_i = -\Delta\varphi_i$, the discrete counterpart of the problem is written as

$$\sum_{k_s=1}^{N_s} A_{i_s k_s}\mu_{k_s} + \sum_{k_v=1}^{N_v} A_{i_s k_v}\mu_{k_v} + \sum_{k_l=1}^{N_l} A_{i_s k_l}\mu_{k_l} + \\ + \sum_{k_s=1}^{N_s} B_{i_s k_s}\sigma_{k_s} + \sum_{k_w=1}^{N_w} A_{i_s k_w}\mu_{k_w} = 0 \ , \quad \forall i_s = 1, \ldots, N_s \ , \quad (10)$$

where A_{ik} and B_{ik} represents the induced potential of the k^{th} doublet and source panel at the point $\boldsymbol{r}_i$,

$$\begin{aligned} A_{ik} &= -\int_{S_k} \hat{\boldsymbol{n}}_{k_s} \cdot \boldsymbol{\nabla}_{\mathbf{0}} G(\boldsymbol{r}_{\mathbf{0}}, \boldsymbol{r}_i)\ dS(\boldsymbol{r}_{\mathbf{0}}) \\ B_{ik} &= -\int_{S_k} G(\boldsymbol{r}_{\mathbf{0}}, \boldsymbol{r}_i)\ dS(\boldsymbol{r}_{\mathbf{0}})\ . \end{aligned} \tag{11}$$

except for the self-induction potential of a doublet,

$$A_{i_s i_s} = E(\boldsymbol{r}_{i_s}) - \int_{S_{i_s}} \hat{\boldsymbol{n}}_{i_s} \cdot \boldsymbol{\nabla}_{\mathbf{0}} G(\boldsymbol{r}_{\mathbf{0}}, \boldsymbol{r}_{i_s})\ dS(\boldsymbol{r}_{\mathbf{0}}) = \frac{1}{2}\ . \tag{12}$$

Note that Eq. (12) is valid only if the surface of the panel S_{i_s} is flat, i.e. the vertices of the panel lie in the same plane. While this condition is always true for triangles, quadrilaterals might have an out of plane distortion. However, if good to high quality meshes characterised by slightly distorted elements are considered, Eq. (12) can be considered valid with a quite good approximation.

At each time step, the intensity σ_{k_s} of the sources is provided by boundary condition in Eq.(9), the intensity μ_{k_w} of the wake doublet elements is known from previous time steps while the doublet intensity μ_k of the surface elements is obtained by solving the linear system obtained by solving (10) with the problems for the other types of elements.

If the surface panels are used to model a lifting object the code can automatically detect the presence of trailing edges, even in case of not completely closed trailing edges. A panel wake is shed from the identified trailing edge in flow direction. At each time step a new panel is released from the trailing edge and its intensity is set to enforce the Kutta condition at the trailing edge, while the rest of the panels are advected with the flow. More details on the wake treatment are presented in Secs. 2.5 and 2.6.

2.3. Vortex lattice (VL)

Thin lifting bodies can be modelled as a zero-thickness two-dimensional vortex sheet S_v, where non-penetration boundary condition,

$$\hat{\boldsymbol{n}} \cdot \boldsymbol{u}_{\varphi} = \hat{\boldsymbol{n}} \cdot (\boldsymbol{u}_b - \boldsymbol{U}_{\infty} - \boldsymbol{u}_{\psi}) =: \sigma \qquad \text{on } S_v \ , \tag{13}$$

must hold. Vortex lattice method provides the aerodynamic elements for the discrete representation of the mean surface of thin lifting bodies, modelled as a sheet of vortex rings of intensity Γ_{i_v}, equivalent to a piecewise-uniform surface doublet distribution with the same intensity $\mu_{i_v} = \Gamma_{i_v}$, $i_v = 1, \ldots, N_v$, [27, sec.10.4.3]. The boundary condition (13) written at every panel collocation point $\boldsymbol{r}_{i_v}$, once made explicit the contribution to the velocity due to all the singular elements, leads to the formulation of the following Eq.

$$\begin{aligned} \sum_{k_s=1}^{N_s} C_{i_v k_s} \mu_{k_s} + \sum_{k_v=1}^{N_v} C_{i_v k_v} \mu_{k_v} + \sum_{k_l=1}^{N_l} C_{i_v k_l} \mu_{k_l} + \\ + \sum_{k_s=1}^{N_s} D_{i_v k_s} \sigma_{k_s} + \sum_{k_w=1}^{N_w} C_{i_v k_w} \mu_{k_w} = \sigma_{i_v} \ , \quad \forall i_v = 1, \ldots, N_v \ , \end{aligned} \tag{14}$$

where C_{ik} and D_{ik} represents the induced velocity of the k^{th} doublet and source panel at the point $\boldsymbol{r}_i$,

$$\begin{aligned} C_{ik} &= -\hat{\boldsymbol{n}}_i \cdot \boldsymbol{\nabla} \int_{S_k} \hat{\boldsymbol{n}}_k \cdot \boldsymbol{\nabla}_{\mathbf{0}} G(\boldsymbol{r}_{\mathbf{0}}, \boldsymbol{r}_i) \ dS(\boldsymbol{r}_{\mathbf{0}}) \\ D_{ik} &= -\hat{\boldsymbol{n}}_i \cdot \boldsymbol{\nabla} \int_{S_k} G(\boldsymbol{r}_{\mathbf{0}}, \boldsymbol{r}_i) \ dS(\boldsymbol{r}_{\mathbf{0}}) \ . \end{aligned} \tag{15}$$

The equations (14) for each vortex lattice panel, added to the (10) for surface panels lead to a linear system for the mixed formulation which will be detailed in Sec. §2.6.

Similarly to what described in Sec. 2.2 for surface panels, vortex lattice elements shed a wake from their trailing edge. At each time step a wake

panel is released in the flow direction from the trailing edge panels, with intensity equal to the one of the trailing edge panel itself to enforce the Kutta condition.

2.4. Lifting Lines (LL)

A lifting line is a 1-D model of thin slender lifting bodies, whose sectional aerodynamic coefficients of lift, drag and moment c_ℓ, c_d, c_m are provided as a function of the local angle of attack α, the local Reynolds number Re and the local Mach number M,

$$\{c_\ell,\, c_d,\, c_m\} = f(\alpha, Re, M; \boldsymbol{r}) \ . \tag{16}$$

The circulation $\Gamma_l(\boldsymbol{r}, t)$ of the lifting line is determined as the solution of a nonlinear problem, connecting $\Gamma_l(\boldsymbol{r}, t)$ with the tabulated aerodynamic coefficients of its lifting sections.

Both a loosely-coupled α-method [28] and a Γ-method [29] solver are available.

In the α-method the angle of incidence resulting from the induced velocity field is used to find aerodynamic coefficients using the enter tabulated aerodynamic tables. In the Γ-method, circulation is computed using tabulated sectional lift and its analytical expression from Kutta-Joukowski theorem. Given the intensity of the other panels (SP and VL), the wake and the body motion conditions, the discrete representation of both methods can be formally formulated as a fixed point problem,

$$\mu_{i_l} = f_{i_l}(\mu_{k_s}, \mu_{k_v}, \mu_{k_l}, \sigma_{k_s}, \mu_{k_w}), \quad i_l = 1, \ldots, N_l \ . \tag{17}$$

A subdivision into a series of uniform-circulation lifting line elements provides a discrete representation of a lifting line component. Each lifting line element with circulation Γ_{i_l} is modelled as a vortex ring composed by the lifting line

segment along with its trailing vortices and the last line vortex released in the wake aligned with the spanwise direction (see Fig. 2). The vortex ring is as wide as the lifting line segment and as long as the airfoil chord. This vortex ring of intensity Γ_{i_l} is equivalent to a uniform surface doublet panel, $\mu_{i_l} = \Gamma_{i_l}$. The set of these lifting line rings form the surface S_l. The grouping of the very first portion of the wake (i.e. the cited trailing vortices and line vortex) with the lifting line into a single element introduces a series of simplifications in the code, primarily from a geometrical standpoint. However, no particular boundary condition is imposed on those element, differently from what is done on vortex lattice elements. As illustrated in Fig. 2, the remaining wake panels are released from the panel comprising the lifting line and the first portion of the wake. The first released panel takes the intensity of the lifting line and of the first portion of the wake at the previous time step, and then in the following time steps is advected with the flow.

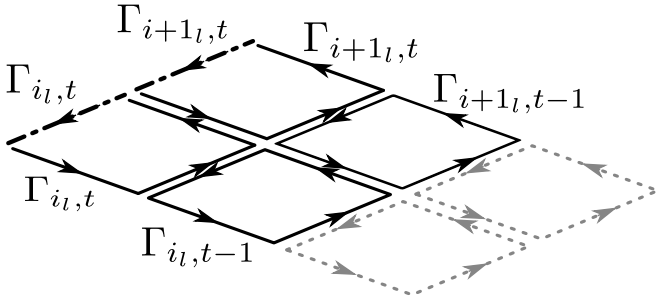

Figure 2: Structure of the lifting lines. In front, dash-dotted, the actual lifting lines segments. Behind, the first portion of the wake composed by the two trailing vortices and the spanwise vortex, which all together form a vortex ring. Following the first vortex ring, composed by the lifting line and the first wake segment, lies the rest of the wake, with a new panel shed at each time step.

Note that while the solution of lifting lines is fully integrated in unsteady time stepping evolution of the combined formulation here described, their

solution is based on the interpolation of aerodynamic coefficients obtained from steady state simulations or experiments. Thus, the user should be aware that the accuracy might degrade in case of extremely unsteady conditions.

2.5. Wake and rotational velocity - Vortex Particle Method

In the potential formulation, wake is shed from the trailing edges of the lifting bodies. When wake is shed from lifting bodies, it is modeled as a panel wake, which shares the same formulation as vortex lattice elements in terms of geometry and singularity distribution. However, the intensity of the panel wake is obtained enforcing the Kutta condition at the trailing edges at each time step, unlike the intensity of vortex lattice elements that is obtained as a solution of the linear problem resulting from the imposition of the non-penetration boundary condition. Details on the enforcement of Kutta conditions are presented in Sec. 2.6. When advected downstream, the panel wake can be converted into vortex particles in order to obtain a more robust wake formulation.

The rotational part of the velocity $\boldsymbol{u}_{\boldsymbol{\psi}}(\boldsymbol{r}, t)$ is produced by line vortices and vortex particles used to model free vorticity in the domain with a mixed panel-vortex particle model of the wake.

The vorticity field $\boldsymbol{\omega}(\boldsymbol{r}, t)$ is the curl of the rotational velocity fields and acts as a volume forcing of the Poisson Eq. (3) for the vector potential $\boldsymbol{\psi}$. Using Green's function method, the vector potential and the rotational velocity can be expressed as a function of the vorticity field as,

$$\begin{aligned} \boldsymbol{\psi}(\boldsymbol{r}, t) &= \int_{\Omega_f} G(\boldsymbol{r}, \boldsymbol{r_0})\, \boldsymbol{\omega}(\boldsymbol{r_0}, t)\; dV(\boldsymbol{r_0}) \;, \\ \boldsymbol{u}_{\boldsymbol{\psi}}(\boldsymbol{r}, t) &= \boldsymbol{\nabla} \times \boldsymbol{\psi} = \int_{\Omega_f} \boldsymbol{K}(\boldsymbol{r}, \boldsymbol{r_0}) \times \boldsymbol{\omega}(\boldsymbol{r_0}, t)\; dV(\boldsymbol{r_0}) \;, \end{aligned} \tag{18}$$

where $\boldsymbol{K}(\boldsymbol{r}, \boldsymbol{r_0}) = \boldsymbol{\nabla} G(\boldsymbol{r}, \boldsymbol{r_0})$ is the Biot–Savart kernel (see e.g. [30]).

The vortex particle method (VPM) provides a Lagrangian grid-free approximation of the vorticity field, as the sum of the contribution of vortex particles of intensity $\boldsymbol{\alpha}_p(t)$ and position $\boldsymbol{r}_p(t)$,

$$\boldsymbol{\omega}(\boldsymbol{r},t) = \sum_{i_p=1}^{N_p} \boldsymbol{\alpha}_{i_p}(t)\,\zeta(\boldsymbol{r}-\boldsymbol{r}_{i_p}(t)) \;, \tag{19}$$

where $\zeta(\boldsymbol{r})$ is a cut-off function determining the distribution of the vorticity induced by the vortex particles, while the rotational velocity field becomes

$$\boldsymbol{u}_{\boldsymbol{\psi}}(\boldsymbol{r},t) = \sum_{i_p=1}^{N_p} \boldsymbol{K}_{\zeta}(\boldsymbol{r},\boldsymbol{r}_{i_p}(t)) \times \boldsymbol{\alpha}_{i_p}(t) \;, \tag{20}$$

where $\boldsymbol{K}_{\zeta}(\boldsymbol{r},\boldsymbol{r}_p)$ is the consistent velocity kernel, determined by the choice of the cut-off function $\zeta(\boldsymbol{r})$ [11].

The evolution of the vorticity field $\boldsymbol{\omega}(\boldsymbol{r},t)$ is governed by the vorticity Eq. (4). The vortex particle method provides a Lagrangian discrete approximation of the vorticity field, through the dynamical equations of the position $\boldsymbol{r}_{i_p}(t)$ and the intensity $\boldsymbol{\alpha}_{i_p}(t)$ of the vortex particles (see [10]),

$$\begin{cases} \dfrac{d\boldsymbol{r}_{i_p}}{dt} = \boldsymbol{u}(\boldsymbol{r}_{i_p}(t),t) \\ \dfrac{d\boldsymbol{\alpha}_{i_p}}{dt} = \boldsymbol{\nabla}\boldsymbol{u}(\boldsymbol{r}_{i_p}(t),t)\cdot\boldsymbol{\alpha}_{i_p} + \nu\ \text{“}\Delta\boldsymbol{\alpha}_{i_p}\text{”} \end{cases} \tag{21}$$

for all the particles, $i_p = 1,\ldots,N_p$. The first equation describes the convection of the i_p^{th} material vortex particles transported by the local flow velocity, while the latter equation describes the influence of vortex stretching-tilting and vortex diffusion on the intensity of the vortex particle. In Eq. (21), vortex stretching-tilting is formulated with a transpose scheme [11], while the quotation marks indicate the need for a model of the diffusion term, since the intensity of the i_p^{th} particle $\boldsymbol{\alpha}_{i_p}(t)$ is not a function of space, therefore its Laplacian is meaningless. The particle strength exchange method (PSE) is

used here, exploiting the approximation of the Laplacian operator with an integral operator, whose discrete counterpart involves the sum of short-range particle interactions (see e.g.[31]).

The vortex particles are generated from the wake vortex lattices. After a prescribed n_{wp} number of time steps, the wake panel is converted into a particle, generating after the initial transient a wake with n_{wp} rows of panels attached to the trailing edges followed by a particles wake. A full particles wake can be obtained by prescribing $n_{wp} = 1$, which leaves only the first row of implicit wake panels.

When converting each panel into a particle the intensity comes from the integration of the vorticity contribution from the sides of the vortex lattice element. However, since each vortex ring panel has a constant intensity and represents a closed path, the simple integration of its sides would lead to a null value. For this reason the actual intensity of each side due to the superimposition of the neighbouring panels sides is considered, and the contribution of each side is distributed to the neighbouring particles which are about to be generated, see Fig. 3 for a detailed scheme. While the neighbouring elements in the direction normal to the flow are converted simultaneously and their contribution is shared with the respective particles, the previous panel in the streamwise direction was already converted the previous timestep. For this reason each particle is formed with the contribution from the two lateral sides of the panel, the rearmost side and a line vortex left by the previous panel, while the present panel leaves the foremost side as a line vortex attached to the following panel. The contribution from each lateral side can be defined as

$$\boldsymbol{J}_s = \begin{cases} \displaystyle\int_s \frac{1}{2}(\mu_{w,i} - \mu_{w,i_n}) d\boldsymbol{l} & \text{if neighbour } i_n \text{ present} \\ \displaystyle\int_s \mu_{w,i} d\boldsymbol{l} & \text{if neighbour } i_n \text{ absent} \end{cases}, \tag{22}$$

where s is one side and the contribution is the whole vorticity of the side if no neighbour is present or half of the net contribution of the side. The other half will be assigned to the neighbouring particle. The end side contribution is

$$\boldsymbol{J}_E = \int_s (\mu_{w,i} - \mu_{i_{end}}) d\boldsymbol{l} \tag{23}$$

where $\mu_{i_{end}}$ is the intensity of the corresponding end line vortex, and thus defining $\boldsymbol{J}_L, \boldsymbol{J}_R$ the contribution from the two lateral sides, the intensity of the generated particle is:

$$\boldsymbol{\alpha_{i_p}} = \boldsymbol{J}_L + \boldsymbol{J}_R + \boldsymbol{J}_E. \tag{24}$$

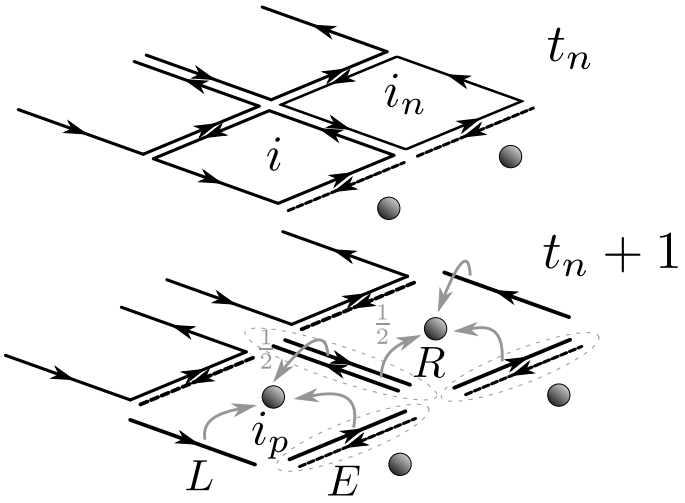

Figure 3: Schematics of an example of conversion from panels to particles: the panel i is converted into the particle i_p, the intensity of the particle is obtained considering the contribution of three sides. The left side L contribution is full since there are no neighbours. The contribution of the end side E is the difference between the panel intensity and the line vortex intensity. The contribution of the right side R is due to the difference between element i and the neighbouring element i_n, however the contribution is split in half between particle i_p and the particle generated by the neighbouring panel.

The newly generated particle is positioned at the centre of the previous panel, and then starts evolving according to (21). Both the computation of

the intensity and the initial placement are approximations, however they do not introduce a significant error, while using more complex distribution of particles to describe a converted panel does not lead to a noticeable increase in accuracy.

The interaction of the particles of the wake with other solid bodies is essential to represent interactional aerodynamics phenomena. The main advantage of a non-structured particles wake without connectivity is that when interacting with a body the stream of particles can divide and pass on the two sides of the object without any interconnecting vortex crossing the structure potentially inducing instabilities. The velocity field induced by the singularities on the body surface should also ensure that the particles do not penetrate the body. However, this is only true for a continuous representation of the unknowns both in time and space, and the discretization both on the surface and in the time integration leads to a possible penetration of the particles in the bodies. In case of severe interactions where the event of penetration is more likely, the user can turn on an explicit non-penetration enforcement. The particles close to the surfaces are checked during the time integration and if during the time step they may cross a surface panel, their velocity is altered to ensure that they remain on the external side of the body.

The computation of particle interactions is accelerated by a Cartesian Fast Multipole Method (FMM) [32], aiming at reducing the computational cost from the $\mathcal{O}(N^2)$ cost of the direct computation of the N particle interactions to the $\mathcal{O}(N)$ cost of the FMM evaluation, in the ideal case. An adaptive Octree structure generates a background hierarchical decomposition of the domain into clusters of cells and the interactions between clusters of well separated particles are evaluated with the Cartesian FMM, based on a polynomial representation of the Plummer potential and the consistent

Rosenhead kernel, $\boldsymbol{K}_\zeta(\boldsymbol{r}, \boldsymbol{r}_{i_p})$ (see [32]).

2.6. Dynamic system and time evolution

The complete dynamical system is obtained coupling:

1. The computation of the boundary condition $\boldsymbol{\sigma}$ from the free stream, body motion and rotational velocity
2. The solution of the mixed potential-velocity linear system for surface panels and vortex lattices
3. The solution of the nonlinear problem for lifting lines
4. The evolution of the potential panel portion of the wake
5. The evolution of the rotational vortex particles part of the wake

The very structure of the complete system just described, replicating the Helmholtz's decomposition of the velocity field, naturally fits an explicit time-stepping algorithm for time integration, alternately solving for the potential part and the rotational part of the velocity field. The previous list of steps are indeed solved at each time step in the detailed sequence, with each step solving for an unknown component of the whole solution employing the already solved parts of the solution and the ones from the previous time step for the parts yet to be solved.

First the geometry is updated: each component generated by an existing mesh or a parametric input in the preprocessor is placed in the space thanks to a user defined hierarchy of reference frames each one defined with an offset and arbitrary orientation with respect to the parent one. These reference frames can also move with respect to the parent one with any arbitrary user defined roto-translation. Thanks to the hierarchical nature of the reference frames it is possible to reconstruct the position and velocity in space, necessary to compute on the one hand the mutual influence of different panels

and on the other hand the non-penetration boundary conditions.

Given the free stream velocity, the rotational component of the velocity field, the state of the wake and the motion of the solid components of the model, the intensity of the surface doublets are the actual unknowns of the potential problem, obtained combining Eq. (10) and Eq. (14),

$$\begin{bmatrix} \mathsf{A}_{ss} & \mathsf{A}_{sv} \\ \mathsf{C}_{vs} & \mathsf{C}_{vv} \end{bmatrix} \begin{pmatrix} \boldsymbol{\mu}_s \\ \boldsymbol{\mu}_v \end{pmatrix} = - \begin{bmatrix} \mathsf{A}_{sl} \\ \mathsf{C}_{vl} \end{bmatrix} \boldsymbol{\mu}_l - \begin{bmatrix} \mathsf{B}_{ss} & \mathsf{0}_{sv} \\ \mathsf{D}_{vs} & -\mathsf{I}_{vv} \end{bmatrix} \boldsymbol{\sigma} - \begin{bmatrix} \mathsf{A}_{sw} \\ \mathsf{C}_{vw} \end{bmatrix} \boldsymbol{\mu}_w \tag{25}$$

where the vector $\boldsymbol{\mu}_w$ collects the intensity of the wake doublets, the vector $\boldsymbol{\sigma} = (\boldsymbol{\sigma}_s, \boldsymbol{\sigma}_v)$ contains the unperturbed relative normal velocity at the collocation points of surface panels and vortex lattice elements, $\mathsf{0}_{sv}$ is a $N_s \times N_v$ null matrix, and I_{vv} is the $N_v \times N_v$ identity matrix. Matrices A_{xy}, B_{xy}, C_{xy} and D_{xy} collect the aerodynamic influence coefficients of the elements of type y on the elements of type x and come from Eqs. (11),(12),(15). The resulting linear system is then re-ordered to separate the elements that are stationary, whose influence coefficient do not vary during the simulation, and the elements that are in motion. The stationary part is pre-factorized in a block factorization scheme at the computations beginning, then each time step the system is completed with the coefficients of the moving components, the block factorization is finished and the system then solved.

The lifting lines nonlinear problem $\boldsymbol{\mu}_l = \boldsymbol{f}_l(\boldsymbol{\mu}_l; \boldsymbol{\mu}_s, \boldsymbol{\mu}_v, \boldsymbol{\sigma}, \boldsymbol{\mu}_w)$ is then solved using the panels intensities $\boldsymbol{\mu}_s, \boldsymbol{\mu}_v$ just obtained, and once the solution for all the body panels is known the wake is updated.

As introduced earlier lifting bodies release wakes from their trailing edges. Kutta condition represents the vorticity balance at the trailing edge and determines the intensity of the wake panel shed into the domain. Kutta condition is naturally satisfied by vortex lattice and lifting line description of a lifting surface, where the released wake panel has the same intensity as the

vortex ring at the trailing edge [27, sec. 12.3] Differently a row of implicit wake panels is introduced at the trailing edge of thick bodies modelled with surface panels, in order to satisfy the potential jump equivalent to the Kutta condition [27, sec. 12.5]. On each trailing edge location i_{TE} the following condition is imposed:

$$\mu_{w,i_{TE}} = \mu_{s^u,i_{TE}} - \mu_{s^l,i_{TE}} \quad , \quad \boldsymbol{\mu}_{w_{TE}} = \mathsf{T}\boldsymbol{\mu}_s \tag{26}$$

where $\mu_{w,i_{TE}}$ is the first implicit wake panel intensity, while s^u is the SP element with the unit normal approximately aligned with the unit normal vector of the wake surface, s_l is the SP on the opposite side of the trailing edge. The connectivity array T provides the matrix form of the Kutta condition, given the subdivision of the wake intensities in implicit at trailing edge and the rest of the panel wake $\boldsymbol{\mu}_w = (\,\boldsymbol{\mu}_{w_{TE}}, \boldsymbol{\mu}_{\tilde{w}})$.

Equation (26) is enforced directly in the linear system (25), which can be written as

$$\begin{bmatrix} \tilde{\mathsf{A}}_{ss} & \mathsf{A}_{sv} \\ \tilde{\mathsf{C}}_{vs} & \mathsf{C}_{vv} \end{bmatrix} \begin{pmatrix} \boldsymbol{\mu}_s \\ \boldsymbol{\mu}_v \end{pmatrix} = - \begin{bmatrix} \mathsf{A}_{sl} \\ \mathsf{C}_{vl} \end{bmatrix} \boldsymbol{\mu}_l - \begin{bmatrix} \mathsf{B}_{ss} & 0_{sv} \\ \mathsf{D}_{vs} & -\mathsf{I}_{vv} \end{bmatrix} \boldsymbol{\sigma} - \begin{bmatrix} \mathsf{A}_{s\tilde{w}} \\ \mathsf{C}_{v\tilde{w}} \end{bmatrix} \boldsymbol{\mu}_{\tilde{w}}, \tag{27}$$

where the right hand side contribution of the wake is simply reduced to account only for the explicit (already deployed) wake panels, while the modified parts of the matrix are

$$\tilde{\mathsf{A}}_{ss} = \mathsf{A}_{ss} + \mathsf{A}_{sw_{TE}}\mathsf{T} \quad , \quad \tilde{\mathsf{C}}_{vs} = \mathsf{C}_{vs} + \mathsf{C}_{vw_{TE}}\mathsf{T}. \tag{28}$$

After being computed implicitly at the trailing edge the wake panels are advected freely by the flow at each time step, maintaining their intensity, and another set of panels is generated at the trailing edge [27, sec. 13.12].

Finally the vortex particles are generated, if needed, from the wake panels, and the existing particles position and intensity is evolved, generating the rotational velocity field, which stays null until some particles are generated.

2.7. Load computation

The evaluation of the loads acting on the surface of the body depends on the type of the aerodynamic elements used to build the numerical model. If a vortex particle model of the wake is used, the velocity field is not irrotational and thus the Bernoulli principles cannot be applied since no quantity is constant throughout the fluid domain. Following Uhlman [33], inviscid load computation on surface panels relies on the solution of a Poisson's problem for $B = (P - P_\infty)/\rho + (|\boldsymbol{U}|^2 - |\boldsymbol{U}_\infty|^2)/2$, that can be recast using a boundary formulation,

$$
\begin{aligned}
E(\boldsymbol{r})B(\boldsymbol{r},t) - \oint_{S_s} \hat{\boldsymbol{n}}(\boldsymbol{r}_0,t)\cdot\boldsymbol{\nabla}_{\mathbf{0}}G(\boldsymbol{r_0},\boldsymbol{r})B(\boldsymbol{r_0},t)\; dS(\boldsymbol{r_0}) = \qquad & (29)\\
+ \oint_{S_s} G(\boldsymbol{r_0},\boldsymbol{r})\,\hat{\boldsymbol{n}}(\boldsymbol{r_0},t)\cdot\frac{\partial \boldsymbol{u}}{\partial t}(\boldsymbol{r_0},t)\; dS(\boldsymbol{r_0}) + \qquad & \text{(unsteady)}\\
- \int_{\Omega_\varphi} \boldsymbol{\nabla}_{\mathbf{0}}G(\boldsymbol{r_0},\boldsymbol{r})\cdot\boldsymbol{\omega}(\boldsymbol{r_0},t)\times\boldsymbol{u}(\boldsymbol{r_0},t)\; dV(\boldsymbol{r_0}) + & \\
& \text{(rotational)}\\
- \nu \oint_{S_s} G(\boldsymbol{r_0},\boldsymbol{r})\;\hat{\boldsymbol{n}}(\boldsymbol{r_0},t)\cdot\nabla_0^2\boldsymbol{u}(\boldsymbol{r_0},t)\; dS(\boldsymbol{r_0})\;, \qquad & \text{(viscous)}
\end{aligned}
$$

where $\dfrac{\partial \boldsymbol{u}}{\partial t}(\boldsymbol{r_0},t)$ represents the eulerian time derivative. The solution is computed exploiting the matrices A_{ss} and B_{ss} of the potential velocity problem for computing the surface contributions and the vortex particle approximation for computing the volume integral, accelerated by the FMM.

Load computation of the vortex lattice elements relies on the unsteady formulation of the Kutta problem for incompressible flows [34, 35] that is written as follows,

$$
\boldsymbol{F}_i = \rho\boldsymbol{u}_i\times\boldsymbol{l}_i(\mu_i - \mu_{i-1}) - \rho A_i\frac{d\mu_i}{dt}\boldsymbol{n}_i, \tag{30}
$$

where $\boldsymbol{F}_i$ is the force acting on the vortex lattice panel i, $\boldsymbol{l}_i$ is the vector representing the first edge of the vortex lattice panel perpendicular to the free stream direction, $\boldsymbol{u}_i$ is the velocity at the center of such edge and A_i and n_i are respectively the area and the normal vector of the panel. μ_i is the intensity of the doublets of the panel, and in the first term is subtracted by μ_{i-1} which is the intensity of the previous panel in the chordwise direction to obtain the net circulation at the side $\boldsymbol{l}_i$. In case of first panel in chordwise direction, i.e. at the trailing edge, the full intensity of the panel is employed.

Compressibility effects on SP and VL are recovered using the Prandtl–Glauert correction with the associated limitations of the method, i.e. quasi-steady limit.

The evaluation of the aerodynamic loads produced by lifting line elements directly comes as a result of the iterative process. Steady contribution to the loads are evaluated with tabulated steady sectional aerodynamic coefficients $\{c_\ell(\alpha), c_d(\alpha), c_m(\alpha)\}$, while the unsteady contributions are computed with the unsteady version of the Kutta-Joukowski theorem, i.e. using the second term of Eq. (30), as done in [36].

3. Results and Discussion

Numerical simulations were performed with `DUST` over two test cases of unconventional VTOL aircraft that were selected due to the availability of both experimental measurements and high-fidelity numerical simulations. The comparison of `DUST` simulation results over these test cases was aimed at investigating the accuracy and the limits of application of a mid-fidelity approach to capture the aerodynamic performance of complex aircraft configurations. In particular, the first test case consists of a half-span tiltwing tiltrotor model designed at Politecnico di Milano to study the aerodynamic

interaction between wing and rotor in tiltrotor configurations. The scaled model was tested at the large Politecnico di Milano wind tunnel in both hover conditions [23] and in forward flight, at the beginning of a conversion manoeuvre [37]. The second test case, characterised by increasing complexity in the aircraft architecture, is the Vahana tiltwing multirotor eVTOL designed by A^3 by Airbus LLC. Flight tests data were available for this aircraft collected during the Vahana Alpha1 prototype flight test campaign carried out at the flight test range of the Eastern Oregon Regional Ariport in Pendleton, Oregon (The Pendleton UAS Range).

For both the test cases, the high-fidelity CFD simulations were performed with ROSITA (ROtorcraft Software ITAly) code, a finite volume solver of the Reynolds Averaged Navier–Stokes (RANS) equations coupled with the one-equation Spalart-Allmaras turbulence model. The code employed multiple moving multi-block grids to build an overset grid system using the Chimera technique. The details about mathematical formulation of the solver can be found in [4].

3.1. Tiltwing half-span tiltrotor model

The half-span tiltrotor model was composed by a four-bladed rotor, a nacelle and a half-wing with a fixed inner part and an outer part that could rotate around the axis at 25% of the local chord. In the half-model configuration the wing is positioned at a distance of 0.465 rotor radii below the rotor disk. The blade and wing geometry together with the main dimensions of the model and a more detailed description of the experimental set-up can be found in Droandi et al. [38]. The layout of the tiltwing half-model including the reference system used in this work is shown in Fig. 4(a), while a particular of the experimental model is shown in Fig. 4(b).

The high-fidelity CFD simulations for the isolated rotor in hover were

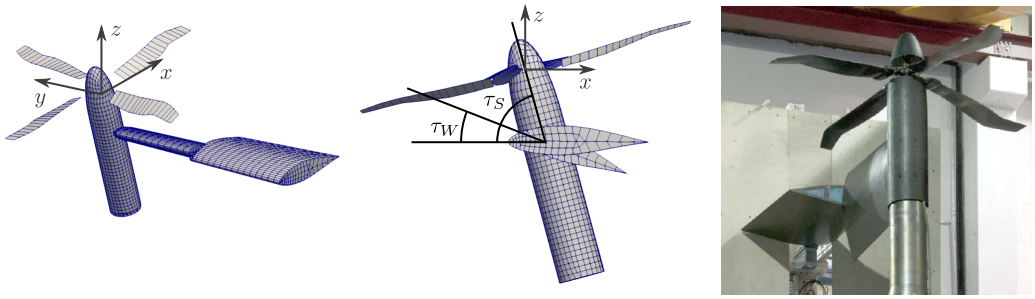

(a) (b)

Figure 4: Tiltwing half-span tiltrotor model: a) layout with reference system as modelled in DUST; b) experimental model in the Politecnico di Milano wind tunnel [38].

performed using a steady state approach with an actuator disk model implemented in ROSITA. Differently, a time-accurate approach was employed for the high-fidelity CFD simulation of the half-span tiltrotor model. The CFD model for the steady state simulations consists of 12.3 million cells while 19.3 millions cells were used for the time-accurate simulation. Due to the very high computational effort required for this approach only one high-fidelity simulation was performed for the half-model configuration (outboard half-wing tilted of $\tau_W = 90°$) reproducing the trim condition of the rotor with $C_T/\sigma = 0.078$ and collective pitch angle $\theta = 12°$. Each steady simulation took about 21–25 hours by running the CFD solver in parallel on 64 processors until the convergence was reached. The time accurate simulation was much more time consuming and took about 44 days to complete 10 rotor revolutions, each of which required about 98 hours to be completed by running the ROSITA code in parallel on 128 processors. The details of the computational models used for the high-fidelity simulations are reported in Droandi et al. [23].

In DUST simulations, the rotor blades were modelled as lifting lines, while the nacelle and the wing are modelled with surface panels to effectively cap-

ture the interactions of the wake with the solid bodies. Each blade was discretized with 16 lifting lines elements, while nacelle and wing were modelled using 2500 surface elements. Simulations were advanced in time with a discretization of 40 timesteps for each rotor revolution. A fully developed wake for these cases consisted of around 10 thousands vortex particles. The discretization parameters represent a choice based on dependence studies performed in a previous work dealing with several simpler tests and with the tiltwing half-model test case [22]. This choice is a compromise to obtain a good accuracy while limiting the computational cost. Indeed, one of the main goal of the present work is to show the capabilities and accuracy of a mid-fidelity approach to be used in the design process of novel complex aircraft configurations, requiring a comprehensive number of test cases to be investigated. Simulations were performed on a workstation with a 18 cores processor. The length of a simulation covers 20 complete rotors revolutions. The simulation took about 2 minutes for an isolated rotor in hover configuration, while the simulation for the half-span model including the rotor, nacelle and wing took around 9 minutes in forward flight and 10 minutes in hover.

3.1.1. Hover condition

Figure 5 shows the convergence in time of the thrust coefficient calculated by `DUST` throughout the simulations for the isolated rotor configuration in hover.

This convergence study shows that for all the tested collective pitch angles, the computed thrust coefficients reach a steady value after around five rotor revolutions. To ensure the complete convergence of the loads and a sufficient averaging interval, all the load values regarding the tiltrotor configuration were averaged between 10 and 20 rotor revolutions from the beginning of the simulations.

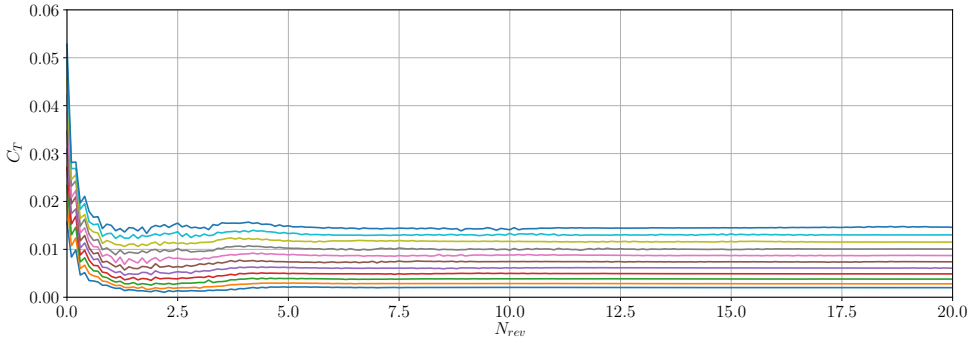

Figure 5: Convergence of the thrust coefficient C_T during the simulation time, as a function of the number of rotor revolutions N_{rev}, for all the tested collective pitch angles of the isolated rotor in hover.

Figures 6 and 7 show the comparison of DUST results with CFD data and experiments, respectively for the isolated rotor and for the half-model configuration with the outboard half-wing tilted of $\tau_W = 90°$ in hover. In particular, for the half-model configuration, in order to consider the real efficiency of the system, the performance comparison was made for the net figure of merit FM^* and the net thrust coefficient C_T^* calculated considering the net thrust of the model T^* as the difference between the rotor thrust and the vertical load acting on the wing.

The mid-fidelity simulations results are in good agreement with the high-fidelity and the experimental results for both the configurations tested. In particular, DUST simulations capture quite well the rotor figure of merit for the higher range of C_T tested, providing the same accuracy obtained by the high-fidelity simulations. The highest discrepancies of the computed FM with respect to CFD and experimental data were found for C_T/σ below 0.05 (see Fig. 6(a) and 7(a)). The discrepancies observed in this range could be related to the fact that the lifting line modelling implemented in DUST does

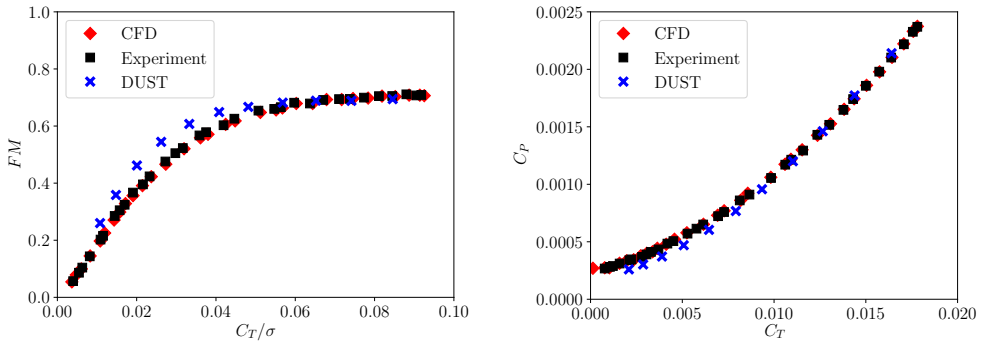

(a) (b)

Figure 6: Comparison of isolated rotor performance in hover: a) FM as a function of C_T/σ, b) C_P as a function of C_T, for $M_{Tip} = 0.32$.

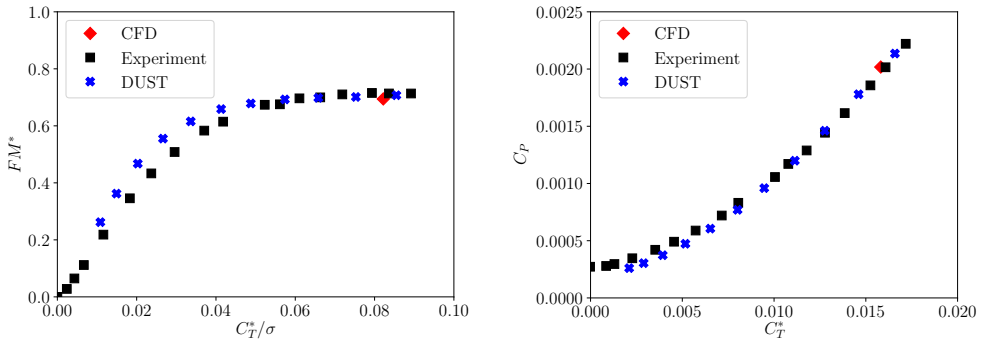

(a) (b)

Figure 7: Comparison of rotor performance for the half-model configuration $\tau_W = 90°$ in hover: a) Net figure of merit FM^* as a function of C_T^*/σ, b) C_P as a function of C_T^*, for $M_{Tip} = 0.32$, where C_T^* is the net thrust coefficient calculated considering the net thrust of the model T^* as the difference between the rotor thrust and the vertical load acting on the wing.

not take into account the thickness contribution. The behaviour of the power coefficient curve with respect to thrust coefficient is quite well captured by `DUST` simulations for both the tested configurations, as can be observed in

Figs. 6(b) and 7(b).

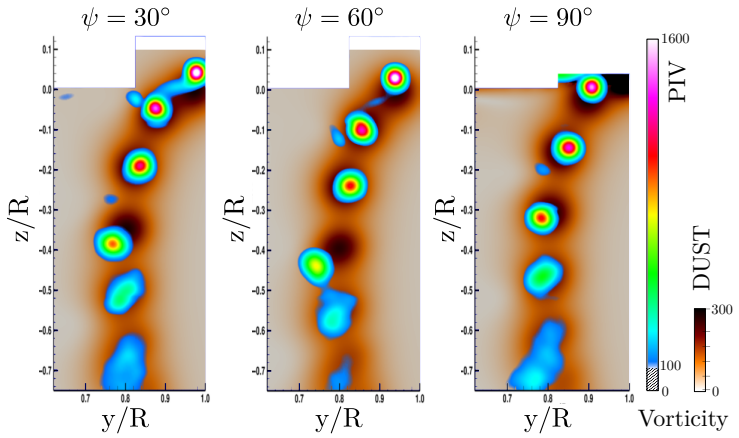

(a) Isolated rotor

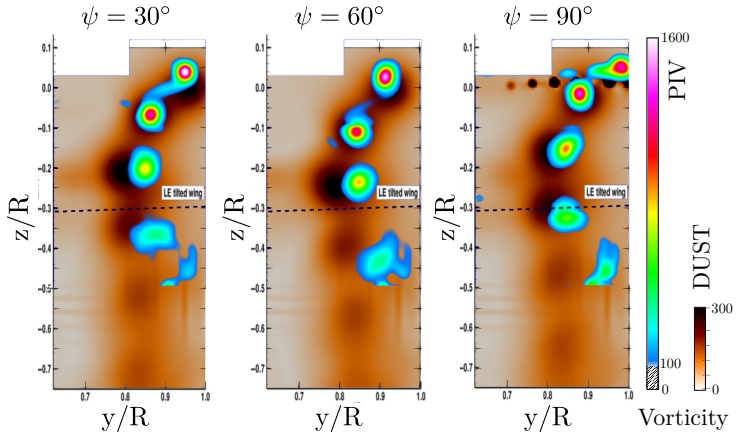

(b) Half-model, $\tau_W = 90°$

Figure 8: Comparison of phase-average out-of-plane vorticity field $\omega_\theta(r, z)$ in an azimuthal plane below the rotor in hover at collective $\theta = 12°$, at different phase angles ψ. The computed vorticity field are shown with a white-orange-black colormap while the experimental field measured by PIV is shown by a rainbow colormap for $\omega_\theta(r, z) > 100s^{-1}$.

In order to evaluate the capability of the mid-fidelity approach to capture the flow physics involved in rotor-wing interaction, Fig. 8 shows the phase-averaged out-of-plane vorticity field contours computed by `DUST` on azimuthal

planes below the rotor compared to PIV measurements [38]. In particular, the flow fields comparison is presented for both the isolated rotor and the half-model in hover with collective pitch angle set to $\theta = 12°$. Moreover, a quantitative comparison of the tip vortex core paths below the rotor is shown in Fig. 9 for the same test condition, where the tip vortex core location was analyzed by identifying the vortex center with the position of the local maximum vorticity. The vortex core positions are plotted for all phase-locked positions surveyed by PIV measurements.

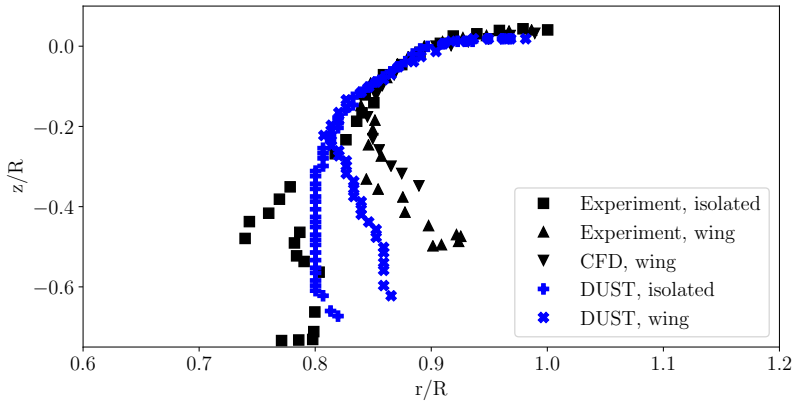

Figure 9: Tip vortex core paths in an azimuthal plane below the rotor in hover, with and without the wing (outboard half-wing tilted $\tau_W = 90°$). Comparison of the DUST computation with the PIV measurements and unsteady CFD computations from Droandi et al. [23]. Blades collective pitch $\theta = 12°$, $M_{Tip} = 0.32$.

For the isolated rotor test case the shape of the rotor wake is well captured by DUST as shown in Fig. 8 for all the three azimuthal positions of the blades. A small discrepancy with respect to experiments is observed for the vortex core position in the region between $-0.4 < z/R < -0.5$ at $\psi = 30°$ and $\psi = 60°$. This local contraction of the wake boundary is related to the instability of the wake helical structure, as discussed in [23]. Nevertheless,

the wake profile evaluated by DUST in the lower region shows a behaviour similar to the average wake boundary measured by PIV, as shown in Fig. 9.

For the half-model configuration, DUST simulations capture well the shape of the upper region of the rotor wake. The wake expansion due to the wing interaction is also captured even if a higher contraction of the wake boundary is observed from experiments with respect to DUST computations starting from $z/R = -0.2$ (see the vortex position in Fig. 8). Nevertheless, the comparison of the vortex paths in Fig. 9 shows a discrepancy below 5% of the rotor radius between DUST and experiments in the lower region of the rotor wake. The high-fidelity CFD retraces quite well the experimental vortex path showing a higher expansion of the wake boundary due to the interaction of the wing. The lower maximum vorticity values shown in Fig. 8 are mainly due to the regularization kernels of the particles which do not have the resolution to capture the vorticity peaks.

A global visualization of the flow field for the half-model configuration in hover is shown in Fig. 10 by means of three-dimensional iso-contours of vorticity and vortex particle distribution of intensities computed by DUST simulations. The interaction between the rotor wake and the tilted outboard half-wing is apparently captured by DUST. Indeed, the vortex structure issued by the rotor blade is broken into two parts approaching the wing leading edge. Consequently, the half-wing interaction destroys the coherence of the vortex structure travelling downstream the wing chord and the associated vorticity is quite diffused. Furthermore, the footprint of the vortex structure interaction with the half-wing is clearly shown by the peaks of the pressure coefficient C_p contours on the wing surface.

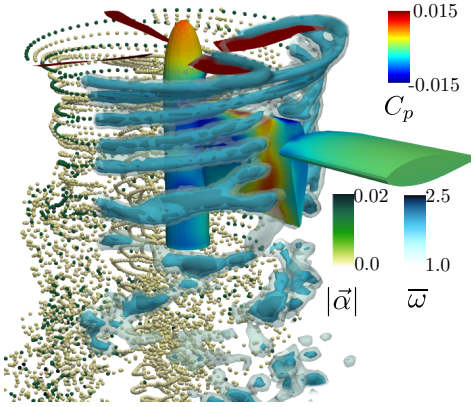

(a) Hover, $\tau_S = 90°, \tau_W = 90°$, $\theta = 12°$

Figure 10: Visualizations of the flow around the rotor and half wing model in hover computed by DUST simulations, $\tau_S = 90°, \tau_W = 90°$, $\theta = 12°$. Surface visualization of tip velocity based pressure coefficient C_p (rainbow scale). On the outboard half of the model the vortex particle distribution of intensities are visualized (green scale), while on the inboard half of the rotor iso-contours of the normalized vorticity are depicted (blue scale).

3.1.2. Forward flight condition

Figure 11 shows the comparison of DUST simulations results with experiments for the forward flight condition tested considering the beginning of a conversion manoeuvre of the tiltrotor [37]. High-fidelity simulations are not available for the present test case due to the high computational cost required for this test conditions that was well beyond the computational capabilities of the research project described in [37].

Figure 11(a) shows the comparison of the isolated rotor performance in forward flight in terms of the power coefficient C_P distribution as a function of the vertical force coefficient C_{Fz} at different shaft angles, i.e. a vertical rotor in a full helicopter configuration and a rotor partially tilted towards the free stream. DUST simulations results are compared with experiments

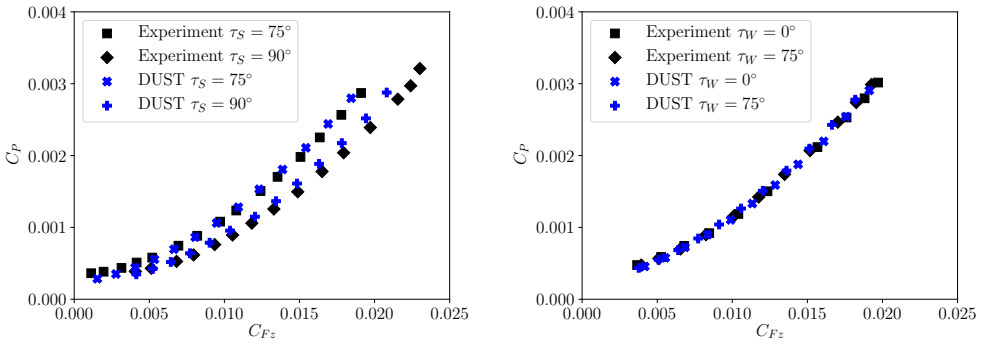

(a) (b)

Figure 11: Comparison of rotor performance in forward flight, C_P as a function of vertical force coefficient C_{Fz}, for advance ratio $\mu = 0.115$: a) isolated rotor at different shaft angles τ_S, b) half-model at shaft angle $\tau_S = 75°$ at different angles of the outboard half wing τ_W.

for two rotor shaft attitudes τ_S defined as the angle between the rotor shaft axis and the free stream velocity direction (see Fig. 4a). For both the test conditions `DUST` simulations capture quite well the rotor performance in the whole range of the collective pitch angles tested. A quite good agreement with experiments is also obtained for the test configurations with shaft attitude $\tau_S = 75°$ at two different angles of the outboard half-wing τ_W, one flat as the inboard and one tilted as the rotor shaft. The very good matching with the experimental results shows the capabilities of the mid-fidelity approach to capture the rotor aerodynamic performance in the first phase of a conversion manoeuvre of a tiltrotor aircraft.

An insight about the flow behaviour characterising the latter flight conditions is provided by the visualization of the flow field shown in Figs. 12(a) and 12(c) for the half-model configuration with the shaft attitude $\tau_S = 75°$. In particular, when the outboard half-wing is not tilted (i.e. $\tau_W = 0°$), the rotor wake is convected by the free stream and is weakly influenced by the

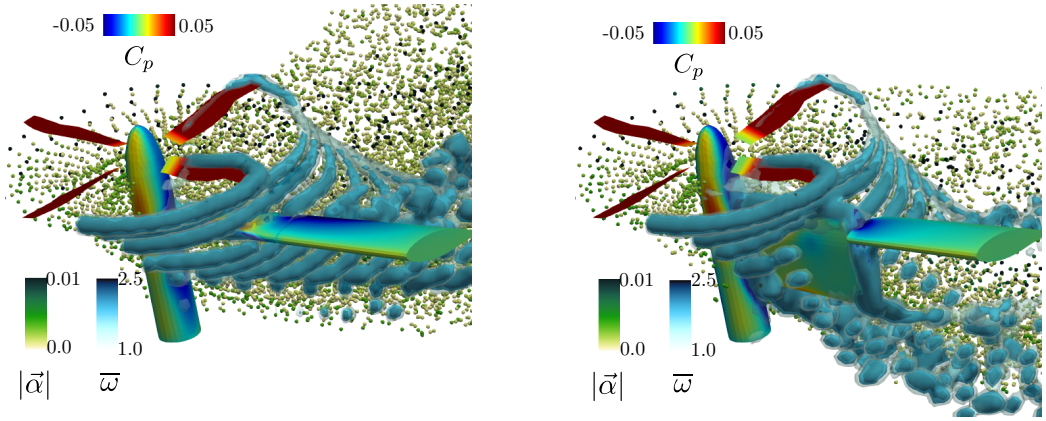

(a) Forward flight, $\mu = 0.115$, $\tau_S = 75°, \tau_W = 0°$, $\theta = 12°$, $\theta_{1S} = -4.6°$, $\theta_{1C} = -1.0°$

(b) Forward flight, $\mu = 0.115$, $\tau_S = 75°, \tau_W = 75°$, $\theta = 12°$, $\theta_{1S} = -4.9°$, $\theta_{1C} = -1.1°$

Figure 12: Visualizations of the flow around the rotor and half wing model computed by DUST simulations. Surface visualization of tip velocity based pressure coefficient C_p (rainbow scale). On the outboard half of the model the vortex particle distribution of intensities are visualized (green scale), while on the inboard half of the rotor iso-contours of the normalized vorticity are depicted (blue scale).

wing interaction, as shown by the quite coherent helical vortex structure depicted by three-dimensional iso-contours of vorticity. On the other hand, for the half-model configuration with the outboard half-wing tilted ($\tau_W = 75°$), the wing effect on the wake is evident. Indeed, the coherence of the helical vortex structure of the rotor wake is quite destroyed past the wing region and vorticity is strongly diffused in this area.

3.2. Tiltwing multirotor eVTOL aircraft

Mid-fidelity simulations results of the Vahana full vehicle are compared in the present section with flight test and high-fidelity CFD data in different flight configurations.

The vehicle is characterised by a tandem tiltwing configuration equipped

with eight fans. A pair of counter-rotating fans is distributed on each side of the canard (i.e. the front lifting surface) and the wing (i.e. the rear lifting surface), with the outer fans located at the lifting surface tips (see the vehicle layout as modelled in `DUST` shown in Fig. 13(a)). A picture of the vehicle prototype used for flight tests is shown in Fig. 13(b).

The flight configurations considered comprise several steady trimmed flight conditions of the eVTOL vehicle. Three helicopter mode configurations, i.e. hover, climb and descent flight, were investigated, alongside two forward flight conditions during the transition maneuver from hover to cruise mode characterised respectively by a velocity of 21.0 m/s and 36.3 m/s.

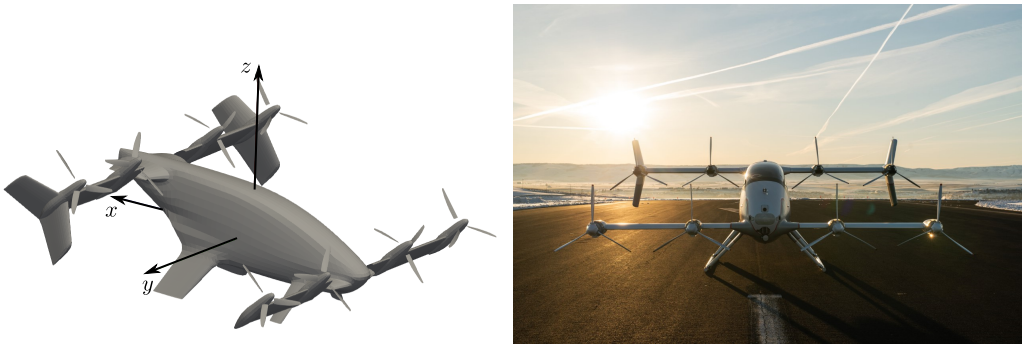

(a) (b)

Figure 13: Vahana tiltwing multirotor eVTOL aircraft: a) layout with reference system as modelled in `DUST`; b) vehicle prototype used for flight tests.

High-fidelity CFD calculations of the full Vahana vehicle were performed with ROSITA solver in steady state approach as reported in the work by Droandi et al. [24]. The rotating fans were modelled using non-uniform actuator disks by means of a simplified three-dimensional cylindrical mesh used for projecting the fan blades on their tip path planes. The vehicle CFD model was made by 68.9 millions cells. The high-fidelity computations were run on a cluster made up of 1008 cores distributed over 56 nodes. For each

analysis, a single iteration took about 4 hours while the total time ranged between 24 and 32 hours depending on the number of iterations needed to achieve loads convergence.

Details regarding the dimensions and geometry of the aircraft as well as about the CFD simulations considered in the following as reference for comparisons with `DUST` can be found in [24].

Mid-fidelity simulations with `DUST` were performed for each flight condition using the vehicle states measured during the corresponding flight test, i.e. canard and wing tilt angles, vehicle pitch angle, fans rotational speed and fan collective pitch setting. No trim analysis was performed to re-trim the vehicle. `DUST` numerical model of the vehicle was built using surface panels for both wings (including motor fairings and spinners) and fuselage, while lifting line elements were employed to model the blades. Fan blades and wings shed a wake at the trailing edge, while the fuselage does not. Each of the 24 fan blades was modelled with 17 lifting lines elements, while a total number of 10838 surface panels were employed to model the fuselage and lifting surfaces. The simulations were discretized in time using 48 timesteps for (canard) fan revolution and lasted for 20 revolutions. A fully developed wake for the Vahana aircraft model consisted of around 540 thousands vortex particles for hover cases and 240 thousands for the forward flight ones. The computational time on an 18-cores workstation was around 7 hours for a complete hover case, and around 5 hours for forward flight cases.

The comparison between the mid- and high-fidelity simulations results and experimental measurements gathered during the flight test campaign are shown by the relative error in the vertical equilibrium of the vehicle defined as,

$$\Delta L = \frac{\Delta L^{num}}{W^{exp}} = \frac{L^{num} - W^{exp}}{W^{exp}} \ , \tag{31}$$

and of the relative error in the longitudinal position of the application point of the aerodynamic forces x_a defined as,

$$\Delta x_a = \frac{x_a^{num} - x_a^{exp}}{c} \tag{32}$$

where the position x_a^{exp} during flight test is evaluated from the trim conditions and c is the reference chord of the canard. As the vehicle center of gravity for the different conditions is known from the flight test data, the Δx_a values provide an indication of the error occurred for the moment evaluation.

3.2.1. Helicopter mode conditions.

For the helicopter mode three different conditions were considered including hover and climb, descent at vertical flight speed $V_z = \pm 2.54\ m/s$. In helicopter mode the wings are tilted almost vertically and the required lift is generated only by the eight fans. The wings provide only a small contribution to force, mainly due to the interaction with the fans downwash. Such a small contribution, while playing a negligible role in vertical equilibrium, affects, however, the equilibrium about the pitch axis and contributes to vehicle authority around yaw axis.

Figure 14 shows the ΔL and Δx_a errors of `DUST` and high-fidelity CFD simulations for the helicopter mode flight conditions.

For hover condition `DUST` and ROSITA predictions show a quite good agreement with flight test data. Higher differences can be observed in climb and descent concerning vertical force calculation, see Fig. 14(a). In particular, in descent flight condition `DUST` computations slightly overestimates the vehicle total vertical force of about about 6.5%, while in climb condition the

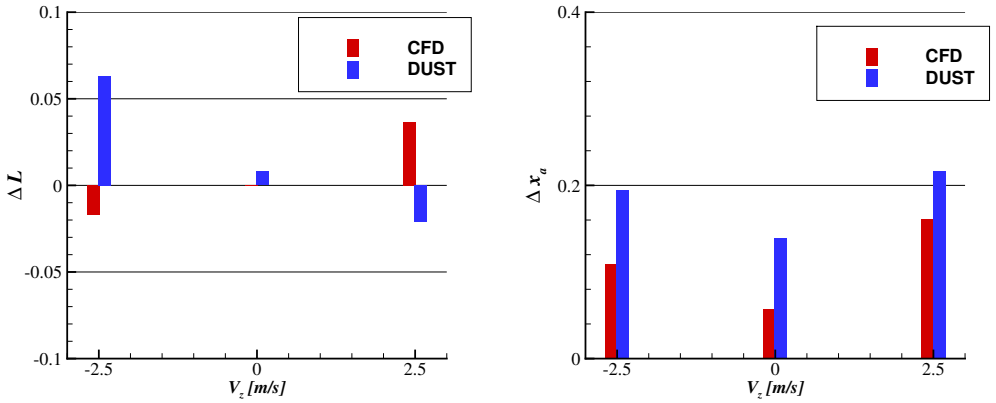

(a) (b)

Figure 14: Vahana full vehicle in helicopter mode. Difference between numerical simulations results and the flight test data in hover, climb and descent conditions. (a) Vertical force, (b) longitudinal position of the application point of the aerodynamic forces based on pitching moment equilibrium.

vertical force is underestimated of about 2%. High-fidelity simulations results for climb and descent conditions show an opposite trend of the vertical force with respect to `DUST` computation but with a relative error of the same order.

Considering the pitching moment equilibrium, the trend of the relative error based on `DUST` predictions is similar to the error computed using high-fidelity CFD. As shown in Fig. 14(b), `DUST` results show a slightly higher error with respect to hi-fi CFD for all the three flight conditions in helicopter mode. These differences should be related to an incorrect prediction of the aerodynamic effects induced by fuselage and lifting surfaces on the fans. Indeed, these flight conditions are characterised by low velocities and low Reynolds numbers, thus the corresponding complex flow conditions have to be considered difficult to be represented with potential methods. This complex flow behaviour around the vehicle in hover condition can be appre-

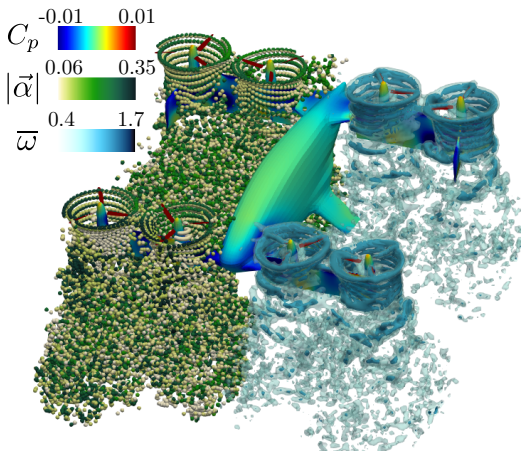

Figure 15: DUST simulation of Vahana Alpha in hover. Surface visualization of pressure coefficient C_p based on rotor tip velocity, in rainbow scale. Right side of the vehicle: visualization of the wake particles with intensity, in green scale. Left side of the vehicle: iso-contours of vorticity, in blue scale.

ciated by the visualization reported in Fig. 15.

3.2.2. Airplane mode conditions.

The first condition analyzed in forward flight corresponds to a flight conditions during the transition maneuver with moderate-speed, i.e. $V_\infty = 21.0\ m/s$. This flight condition is characterised by large tilt angles of the wings, small blade collective pitch angle and a small vehicle angle of attack. The main lifting surfaces in this condition operate beyond stall thus they do not produce enough lift to sustain level flight. Canard and wing fans are, hence, used to provide both lift to sustain level flight and pitching moment to trim the vehicle about the pitch axis. Canard and wing fans spin at different rotational speed to provide the required differential thrust.

Figure 16 shows the comparison between `DUST` and CFD numerical results with flight test data for both the airplane mode conditions tested.

For the flight condition characterised by moderate speed, high-fidelity

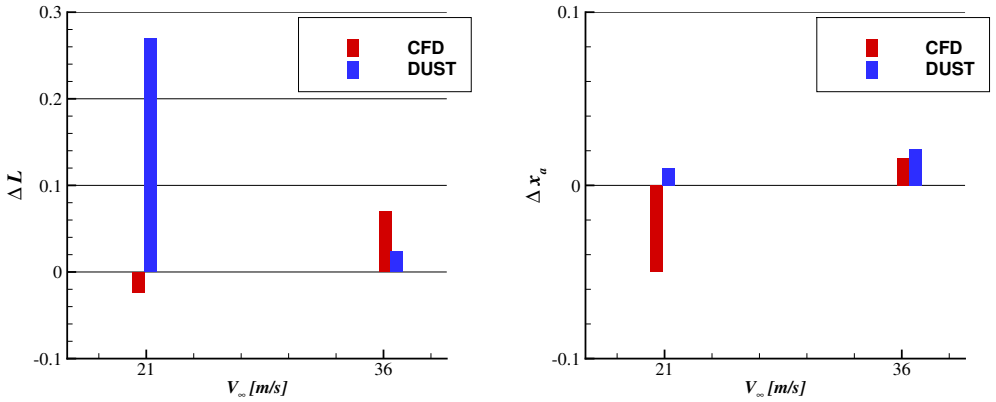

(a) (b)

Figure 16: Vahana full vehicle in airplane mode. Difference between numerical simulations results and the flight test data. (a) Vertical force, (b) longitudinal position of the application point of the aerodynamic forces based on pitching moment equilibrium.

CFD results match quite well the trim condition measured during flight test both for vertical force and pitching moment. The error in the vertical equilibrium obtained with CFD is below 5% in absolute value, while `DUST` overestimates by 27% the vertical force provided by the full vehicle. This is likely to be related to the fact that surface panels are not capable to describe properly the stall of the main lifting surfaces. On the other hand, a fairly good estimate of the vehicle pitching moment is obtained by `DUST`. The latter result could be related to the fact that there is a similar lift overestimation on both the canard and the main wing, leading to an increased overestimation of the lift but also to a mutual compensation of the pitching moment evaluation with respect to flight test data. Moreover, the evaluation of the pitching moment is also affected by drag prediction on both the fuselage and the stalled lifting surfaces.

An insight about the aerodynamic interaction characterising this flight condition is obtained by the flow visualization around the vehicle depicted in

Fig. 17(a) by the isosurfaces of vorticity magnitude. The flow visualization highlights the strong aerodynamic interaction between the fans and the lifting surfaces in this flight condition. In particular, each fan generates a vortex wake system that impinges on the underlying lifting surface. The rapid loss of coherence of the vortices generated by the fan blade tips when advected against the tilted lifting surfaces indicates the stronger aerodynamic interactions that characterise this flight condition with respect to the faster flight condition described in the following (see the visualization in Fig. 17(b)).

The second analyzed condition in airplane mode corresponds to a flight condition in the last part of the transition maneuver with a higher speed of $V_\infty = 36.3\ m/s$. This flight condition is characterised by small wings tilt angles, a relatively high blade collective pitch and different rotational speed between the canard and wing fans. The vehicle trim about the pitch axis is obtained through differential thrust from the fans, while lift is mainly generated by the wings. The contribution of the fans to the vertical equilibrium is marginal in this flight condition due to the small tilt angles of the fans and to the moderate angle of attack of the vehicle. In fact, the fans axes are almost aligned with the free stream.

In this flight condition, both `DUST` and high-fidelity CFD simulations results match quite well the trim condition measured during flight test (see Fig. 16). In particular, `DUST` provides the same accuracy of high-fidelity CFD results for both the vertical force and pitching moment, but obtained with a calculation time orders of magnitude lower.

An insight about the flow physics characterising this second flight condition is presented by Fig. 17 (b), that illustrates the flow behavior around the vehicle by means of isosurfaces of vorticity magnitude. The flow visualization shows strong coherent vortex structures shed by the tips of the canard, the

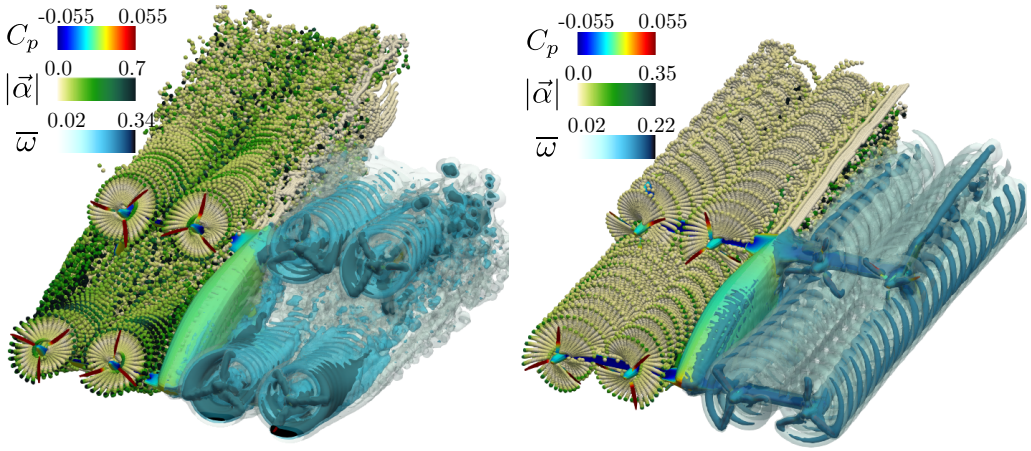

(a) $V_\infty = 21.0\ m/s$ (b) $V_\infty = 36.3\ m/s$

Figure 17: Vahana Alpha in forward flight in transition configuration and at high-speed forward flight. Pressure coefficient C_p contours on the body surface and visualization of the wake with vortex particle distribution of intensities $|\boldsymbol{\alpha}_p|$, on the right side of the vehicle, and vorticity magnitude iso-surfaces on the left side of the vehicle.

tips of the wing, and the winglets. Moreover, a negligible contraction of the fans wake systems is observed due to the low disk loading characterising this condition. Indeed, the fans wake is immediately convected downstream by the free stream velocity.

3.2.3. Shaft power analysis.

The comparison of the shaft power computed by `DUST` and high-fidelity CFD simulations for all the vehicle fans at moderate and high-speed is presented in Fig. 18(a-b). In particular, the rotor power breakdown is shown by the ratio between available power $P_a = TV_\infty \cos\tau_S$ and shaft power $P_s = Q\Omega$ of each rotor. `DUST` and high-fidelity CFD results are in quite good agreement considering almost all vehicle fans. In particular, a discrepancy below 5% is observed for both the analysed flight conditions.

The total shaft power computed by `DUST` and high-fidelity CFD simula-

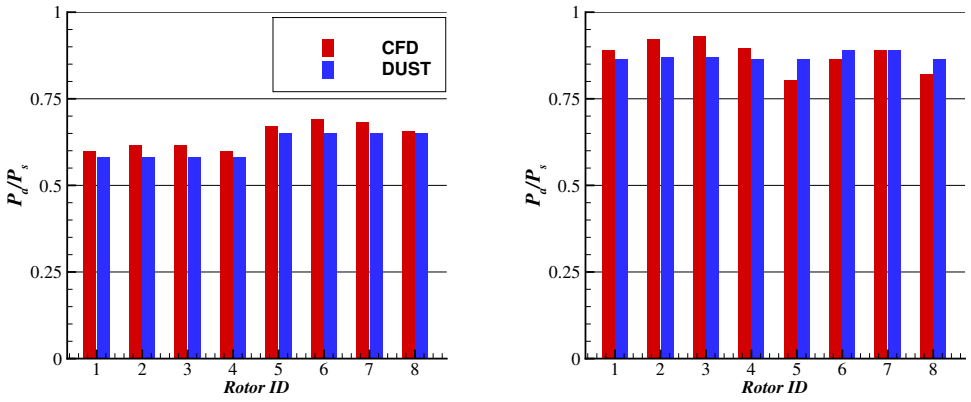

(a) $V_\infty = 21m/s$ (b) $V_\infty = 36.3m/s$

Figure 18: Rotor power breakdown in airplane mode conditions. Rotor ID: 1–4 canard, 5–8 wing, from the left of the vehicle to the right.

tions in both hover and forward flight conditions is compared with flight test data in Fig. 19. In particular, the chart shows the non-dimensional values of the shaft power calculated with respect to the total shaft power measured in hover during the flight test campaign. A quite good evaluation of the measured total shaft power is provided by `DUST` simulations. In particular, in

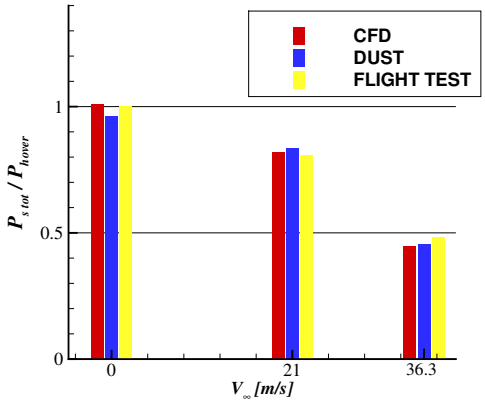

Figure 19: Total shaft power comparison in hover and airplane mode conditions.

hover flight condition DUST slightly underestimates the measured total shaft power (i.e. less than 5%). For the moderate and high-speed flight conditions DUST provides an estimation of the total shaft power in quite good agreement with high-fidelity CFD, showing errors with respect to the measured shaft power of few percents (i.e. less than 3%).

4. Conclusions

A novel open source mid-fidelity aerodynamic tool was recently developed from a collaboration between Politecnico di Milano and A^3 by Airbus LLC with the aim to provide fast and reliable evaluation of unconventional VTOL aircraft aerodynamic performance. The mathematical formulation of DUST is provided in the manuscript for a full dissemination to users. Moreover, the potentialities and the limitations of the mid-fidelity approach implemented in the solver are shown by comparison with high-fidelity CFD simulations results and experimental data obtained over unconventional VTOL aircraft test cases of increasing complexity.

The results comparison shows that, combining aerodynamic elements with different level of fidelity, DUST simulations is capable to represent successfully the aerodynamic performance and flow physics of complex configurations, particularly for flight conditions characterised by limited flow separations. Indeed, surface panels provide quite an accurate model for streamlined solid bodies at small angle of attack, while they fail in describing flow separation and stall, overestimating the lift. Rotor blades modelling is quite accurate using tabulated aerodynamic data of lifting lines, thus providing a simple model of both viscous drag and stall phenomenon. Moreover, the vortex particle modelling of wakes avoids the numerical instabilities occurring typically when using panels models of the wake in practice, thus allowing to

capture the flow physics related to aerodynamic interactions between rotor wakes and solid bodies.

The presented analysis shows that a flexible mid-fidelity aerodynamic tool as `DUST` can be considered a valuable tool to be used for the preliminary design of complex aircraft as eVTOLs. Indeed, the very low computational costs of a mid-fidelity approach for aerodynamics enables to perform a large number of simulations required in the preliminary phase of the aircraft design while providing a quite accurate evaluation of the vehicle aerodynamic performance. In particular, for flight conditions characterised by limited flow separations, mid-fidelity simulations provide a degree of accuracy similar to high-fidelity CFD computations for the evaluation of essential performance parameters as vertical aerodynamic force, pitching moment and total shaft power. These results can be obtained with a computational cost orders of magnitude lower with respect to high-fidelity CFD simulations of complex VTOL vehicles. Moreover, the thorough analysis presented in this work indicates the range of flight conditions where a mid-fidelity approach is suitable for a correct evaluation of the aerodynamic performance of unconventional aircraft and where high-fidelity CFD still represents an essential tool for the detailed design process of the aircraft.

Acknowledgements

This research has received funding from A^3 by Airbus LLC in the frame of a research contract with Politecnico di Milano.

References

[1] L. Cambier, S. Heib, S. Plot, The onera elsa cfd software: input from research and feedback from industry, Mechanics and Industry TP 2013-

437 (2013).

[2] N. Kroll, B. Eisfeld, H. Bleecke, The navier-stokes code flower, Notes on Numerical Fluid Mechanics 71 (1999) 58–71.

[3] M. Biava, M. Woodgate, G. Barakos, Fully implicit discrete-adjoint methods for rotorcraft applications, AIAA Journal 54 (2) (2016) 735–749.

[4] M. Biava, Rans computations of rotor/fuselage unsteady interactional aerodynamics, Ph.D. thesis, Politecnico di Milano (2007).

[5] M. Biava, W. Khier, L. Vigevano, Cfd prediction of air flow past a full helicopter configuration, Aerospace Science and Technology 19 (1) (2012) 3–18.

[6] J. Decours, P. Beaumier, W. Khier, T. Kneisch, M. Valentini, L. Vigevano, Experimental validation of tilt-rotor aerodynamic predictions, in: Proceedings of the 40th European Rotorcraft Forum, Southampton, UK, 2014.

[7] A. Jimenez Garcia, G. Barakos, Cfd simulations on the erica tiltrotor using hmb2, in: Proceedings of the 54th AIAA Aerospace Sciences Meeting, San Diego, CA, USA, 2016.

[8] J. Yin, S. Ahmed, Helicopter main-rotor/tail-rotor interaction, Journal of the American Helicopter Society 4 (2000) 293–302.

[9] M. Wentrup, J. Yin, P. Kunze, T. Streit, J. Wendisch, T. Schwarz, J. Pinacho, K. K, R. Fukari, An overview of dlr compound rotorcraft aerodynamics and aeroacoustics activities within the cleansky2 nacor

project, in: Proceedings of 74th AHS Annual Forum & Technology Display, Phoenix, AZ, USA, 2018.

[10] G.-H. Cottet, P. D. Koumoutsakos, D. Petros, et al., Vortex methods: theory and practice, Cambridge University Press, 2000.

[11] G. S. Winckelmans, Topics in vortex methods for the computation of three-and two-dimensional incompressible unsteady flows, Ph.D. thesis, California Institute of Technology (1989).

[12] T. Su, Y. Lu, J. Ma, S. Guan, Aerodynamic characteristics analysis of electrically controlled rotor based on viscous vortex particle method, Aerospace Science and Technology 97 (2020) 105645.

[13] Y. Lu, T. Su, R. Chen, P. Li, Y. Wang, A method for optimizing the aerodynamic layout of a helicopter that reduces the effects of aerodynamic interaction, Aerospace Science and Technology 88 (2019) 73 – 83.

[14] D. Opoku, D. Triantos, F. Nitzsche, S. Voutsinas, Rotorcraft aerodynamic and aeroacoustic modelling using vortex particle methods, in: Proceedings of the 23rd International Congress of Aeronautical Sciences, ICAS, Toronto, Canada, 2002.

[15] J. Tan, J. Sun, G. Barakos, Unsteady loads for coaxial rotors in forward flight computed using a vortex particle method, Aeronautical Journal 122 (1251) (2018) 693–714.

[16] J. Tan, T. Zhou, J. Sun, G. Barakos, Numerical investigation of the aerodynamic interaction between a tiltrotor and a tandem rotor during shipboard operations, Aerospace Science and Technology 87 (2019) 62–72.

[17] N. Polaczyk, E. Trombino, P. Wei, M. Mitici, A review of current technology and research in urban on-demand air mobility applications, in: Proceedings of VFS Autonomous VTOL Technical Meeting and Electric VTOL Symposium, Mesa, AZ, USA, 2019.

[18] E. Alvarez, A. Ning, Modeling multirotor aerodynamic interactions through the vortex particle method, in: Proceedings of the 54th AIAA Aviation Forum, Dallas, TX, USA, 2019.

[19] DUST - an aerodynamics solution for complex configurations, URL: `https://www.dust-project.org/`.

[20] DUST repository, URL: `https://gitlab.com/dust_group/dust`.

[21] A. Mishra, B. Davoudi, K. Duraisamy, Multiple fidelity modeling of interactional aerodynamics, in: Proceedings of the 35th AIAA Applied Aerodynamics Conference, Denver, USA, 2017.

[22] D. Montagnani, M. Tugnoli, F. Fonte, A. Zanotti, G. Droandi, M. Syal, Mid-fidelity analysis of unsteady interactional aerodynamics of complex vtol configurations, in: 45^{th} European Rotorcraft Forum, Sept. 2019, Warsaw, Poland, 2019.

[23] G. Droandi, A. Zanotti, G. Gibertini, Aerodynamic interaction between rotor and tilting wing in hovering flight condition, Journal of the American helicopter Society 60 (4) (2015) 1–20.

[24] G. Droandi, M. Syal, G. Bower, Tiltwing multi-rotor aerodynamic modeling in hover, transition and cruise flight conditions, in: Proceedings of the 74th Annual Forum, AHS International, Phoenix, 2018.

[25] L. Morino, Helmholtz decomposition revisited: vorticity generation and trailing edge condition, Computational Mechanics 1 (1) (1986) 65–90.

[26] L. Morino, C.-C. Kuot, Subsonic potential aerodynamics for complex configurations: a general theory, AIAA Journal 12 (2) (1974) 191–197.

[27] J. Katz, A. Plotkin, Low-speed aerodynamics, Vol. 13, Cambridge university press, 2001.

[28] S. T. Piszkin, E. Levinsky, Nonlinear lifting line theory for predicting stalling instabilities on wings of moderate aspect ratio, Tech. rep., GENERAL DYNAMICS SAN DIEGO CA CONVAIR DIV (1976).

[29] S. Gallay, E. Laurendeau, Nonlinear generalized lifting-line coupling algorithms for pre/poststall flows, AIAA Journal 53 (7) (2015) 1784–1792.

[30] G. S. Winckelmans, A. Leonard, Contributions to vortex particle methods for the computation of three-dimensional incompressible unsteady flows, Journal of Computational Physics 109 (2) (1993) 247–273.

[31] G. Cottet, S. Mas-Gallic, A particle method to solve the navier-stokes system, Numerische Mathematik 57 (1) (1990) 805–827.

[32] K. Lindsay, R. Krasny, A particle method and adaptive treecode for vortex sheet motion in three-dimensional flow, Journal of Computational Physics 172 (2) (2001) 879–907.

[33] J. S. Uhlman, An integral equation formulation of the equations of motion of an incompressible fluid, Tech. rep., NAVAL UNDERSEA WARFARE CENTER DIV NEWPORT RI (1992).

[34] J. A. Cole, M. D. Maughmer, G. Bramesfeld, M. P. Kinzel, A practical application of an unsteady formulation of the kutta-joukowski theorem, in: 35th AIAA Applied Aerodynamics Conference, 2017, p. 3904.

[35] R. J. Simpson, R. Palacios, J. Murua, Induced-drag calculations in the unsteady vortex lattice method, AIAA journal 51 (7) (2013) 1775–1779.

[36] M. Drela, Integrated simulation model for preliminary aerodynamic, structural, and control-law design of aircraft, in: 40th Structures, Structural Dynamics, and Materials Conference and Exhibit, 1999, p. 1394.

[37] G. Droandi, G. Gibertini, D. Grassi, G. Campanardi, C. Liprino, Proprotor–wing aerodynamic interaction in the first stages of conversion from helicopter to aeroplane mode, Aerospace Science and Technology 58 (2016) 116 – 133.

[38] G. Droandi, G. Gibertini, A. Zanotti, D. Grassi, G. Campanardi, Experimental investigation of the rotor-wing aerodynamic interaction in a tiltwing aircraft in hover, The Aeronautical Journal 119 (1215) (2015) 591–612.